Decipher: A computational pipeline to extract context-specific mechanistic insights from single-cell profiles

Edgar Basto[1,2], Bilal Wajid[1,3,4], James Read[1,5], Jesse Armitage[7,8], Jason Waithman[7,8], Michael Small[2], and Anthony Bosco[1,5,6,†]

[1]Insigene Pty Ltd, Perth, WA, Australia
[2]Department of Mathematics, University of Western Australia, WA, Australia
[3]Ibn – Sina Research & Development Division, Sabz-Qalam, Lahore 54000, Pakistan
[4]Dhani School of Science and Engineering, Habib University, Karachi, Pakistan
[5]Asthma & Airway Disease Research Center, The BIO5 Institute, The University of Arizona, Tucson, AZ
[6]Department of Immunobiology, The University of Arizona College of Medicine, Tucson, AZ
[7]School of Biomedical Sciences, University of Western Australia, WA, Australia
[8]Telethon Kids Institute, WA, Australia

[†]Corresponding author: anthony.bosco@insigene.com

Competing Interests Statement:
AB is the founder of the start-up company INSiGENe Pty Ltd that funded this work. AB is a co-founder, equity holder, and director of the startup company Respiradigm Pty Ltd that is unrelated to this work. EB received a scholarship from INSiGENe Pty Ltd to conduct this work.

List of Abbreviations
BCG – Bacillus Calmette-Guérin (vaccine)
CBMC – Cord Blood Mononuclear Cells
CCC – Cell-Cell Communication
CT – Cell Type
D_{LR} – Decipher Score for Ligand-Receptor Interaction
ERP – Estrogen Receptor Positive
GRN – Gene Regulatory Network
ICB – Immune Checkpoint Blockade
ICU – Intensive Care Unit
IFNG – Interferon Gamma
iSN – Integrated Signalling Network
LR – Ligand-Receptor
ML – Machine Learning
PBMC – Peripheral Blood Mononuclear Cells
pDCs – plasmacytoid dendritic cells
RCT – Receiver Cell Type
SCT – Sender Cell Type
scRNA-seq – Single-cell RNA sequencing
TF – Transcription Factor
TG – Target Gene
TNBC – Triple-Negative Breast Cancer
Δ_{TF} – Change in Transcription Factor activity

Abstract

The advent of single-cell profiling technologies has revolutionized our understanding of the cellular and molecular states that underpin disease states and response to therapies. However, current computational tools cannot recover both known and novel mechanistic insights at distinct layers of biological regulation in an unbiased manner. Here, we present *Decipher*, a novel computational pipeline that builds integrated cell signalling networks from single-cell profiles in a context-specific, data-driven manner and identifies the key cellular and molecular events that drive disease. We benchmarked *Decipher* against existing tools and found

it could recover known, experimentally determined cytokine signalling pathways with high accuracy, whilst maintaining the flexibility to detect novel pathways and context-specific effects. Notably, *Decipher* reports a manageable set of interactions that can be aggregated into global cell-to-cell signalling maps that are interpretable. In addition, we utilised *Decipher* to unveil the cellular and molecular mechanisms driving a novel population of inflammatory monocytes enriched with interferon stimulated genes that is markedly increased in frequency following secondary immunization with the Pfizer-BioNTech COVID-19 mRNA vaccine. Taken together, our findings demonstrate that *Decipher* can decode signalling pathways and report on ligand-receptor mediated transcription factor – target gene networks that underlie processes in homeostasis and disease, as well as cellular responses to therapies. We present *Decipher* as an invaluable new tool for the discovery of novel therapeutic targets and the development of new medicines.

1 Main

Complex multicellular life forms, such as humans, execute a multitude of high-level biological functions, including growth, differentiation, development, organization, metabolism, homeostasis, movement, reproduction, respiration, and digestion. Within the body, such functions are mediated by cell-to-cell interactions[1]. Our understanding of intercellular interactions has recently been transformed by two major technical advances. The first advance has been the development of genomic profiling technologies that enable the profiling of biological systems at single-cell resolution[2]. The second advance has been the development of computational tools that infer cell-to-cell interactions between "sender cells" and "receiver cells" that are mediated by ligand and receptor pairs[3,4]. Inference of cell-to-cell communication from single-cell profiles is an important problem in Systems Biology and an active area of method development. Yet, our current understanding of the underlying mechanisms through which such functions operate within the body in health and disease remains poor, in part, owing to the limitations of existing tools to decipher and quantify the extent of cell-to-cell interactions, as well as their downstream functional consequences[1,5]. Indeed, close to 40 tools have been developed to interrogate cell-to-cell communication. However, most currently available tools suffer from two limitations. The majority of tools interrogate ligand/receptor signaling paths between sender and receiver cells, however they fail to consider the downstream consequences of these signaling events. A subset of more advanced methods take the analysis one step further by modelling the impact of ligand-receptor signaling on the activation of downstream biological responses, some in the form of gene regulatory networks (GRNs) representing the mechanistic regulation of target gene (TG) expression by transcription factors (TFs). These latter tools are typically heavily constrained by prior knowledge which, as a result, limits their capacity to identify novel pathways.

Here, we present a novel computational platform: *Decipher*, which builds integrated cell signaling networks from single-cell profiles and unveils the key cellular and molecular events that drive disease processes and responses to therapies. We demonstrate the application of *Decipher* to single-cell profiling data obtained from diverse experimental settings, and benchmark it against other state-of-the-art methods. We also demonstrate the utility of *Decipher* to extract mechanistic hypotheses from experimental data, highlighting its potential to identify novel therapeutic targets to accelerate the development of new medicines.

2 Results

2.1 – Overview of Decipher

Decipher is a modular pipeline that connects intercellular signalling between ligand/receptor pairs with downstream intracellular responses mediated by transcription factors and their target genes in a data-driven manner (Figure 1). Conceptually, *Decipher* systematically integrates distinct layers of biological

networks to tailor, enrich and extract mechanistic insights based on the context of interest (Supplementary Figure SF.1). Decipher takes as input single-cell (sc) RNA-seq profiles from two experimental conditions along with two prior-knowledge networks: a database of reference Ligand-Receptor (LR) pairs, and a Gene-Regulatory Network (GRN) model. The former delineates which LR pairs have the necessary structural complementarity to interact, whereas the latter informs on known relationships between Transcription Factors (TF) and Target Genes (TG). Here, we use LR pairs from connectomeDB2020[6] and the GRN from CellOracle[7]. Users are welcome to use their preferred prior-knowledge resources depending on their experimental system and setting.

The computational framework underlying *Decipher* is presented in Figure 1. Briefly, *Decipher* employs Seurat for data processing, cell clustering, and annotation. Drop-out effects are reduced by aggregating individual cells into meta-cells[8]. Further, using CellOracle[7], the GRN is pruned to restrict the analysis to edges in the network model that are active in the data set. LR interactions are calculated using a mean-product scoring function that accounts for mean ligand and meta-cell specific receptor expression[6]. TF activity is contrasted across two conditions using an overdispersion-based scoring function (PAGODA[9]) as well as a simple statistical heuristic based on the median expression of each TF in case and control. Here, the change in TF activity is represented by Δ_{TF} .

Thereafter, we merge the tailored LR network and GRN into an integrated signalling network (iSN) to derive data-driven mechanistic relationships between LR pairs and TFs. Our random forest regression-based machine-learning (ML) approach relies on meta-cell LR interaction potential scores and TF activity scores, making use of the importance given to each possible LR-TF interaction as the LR-TF edge weights in our iSN. Additionally, we take the mode of influence of each edge to be the sign of the Spearman correlation of these same scores. This represents one of *Decipher's* primary distinguishing factors, as other methods such as scMLnet[10] rely on further prior-knowledge (such as protein-protein interaction databases) to infer relationships between entities. By deriving data-driven interactions, we allow for LR-TF mechanistic relationships that are novel and/or context specific.

We use this iSN, along with the intracellular responses represented by the TF deltas (Δ_{TF}) calculated previously, to predict which LR pairs are actively responsible for the observed changes in TF activity and, by extension, for the observed cellular response. To do so, we rely on a third scoring function:

$$D_{LR} = \sum_{TF \in TFs} (w_{LR-TF} \cdot \Delta_{TF})$$

where D_{LR} represents the *Decipher* score for an LR interaction. Here, the change in TF activity Δ_{TF} is weighted by the calculated LR-TF relationship weights w_{LR-TF} and summed over all TFs. Thereby, these LR activity predictions presented as our *Decipher* scores explicitly account for both the relationships between intercellular signalling potential and TF activity (through the data-derived LR-TF weights) and for changes in intracellular TF activity across two conditions.

Finally, these scores are visually presented in conjunction with LR statistics and LR-TF relationships to allow the user to extract mechanistic insights about the cellular and molecular responses to a perturbation driven by the regulatory circuits of the system of interest. Based on this design, *Decipher* is a computational method for cell-cell communication analysis that leverages prior-knowledge biological networks and data-driven inference methods to represent the system as an integrated network, and thereby has the capability of identifying active signalling pathways based on their intracellular effects.

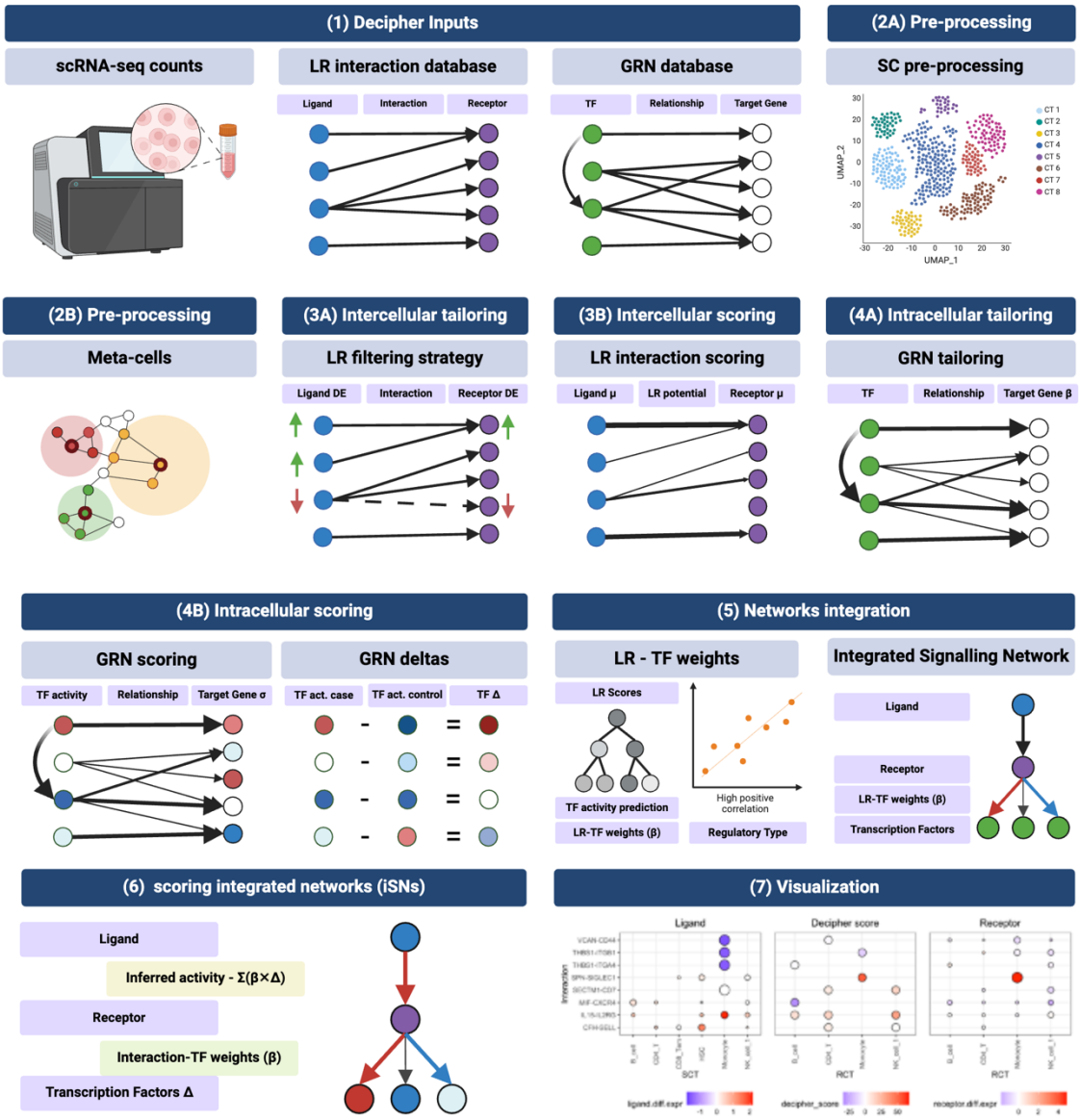

Figure 1 – *Decipher*, a pipeline for modelling inter – cellular communication. *Decipher's* modular pipeline comprises seven primary layers – some with multiple components. **(1)** *Decipher* relies on three inputs, scRNA-seq count data, an LR interaction database and a reference GRN. **(2A)** generally, we assume the user has performed standard pre-processing and cluster labelling on the scRNA-seq count data, if that is not the case, we delineate a standard pre-processing pipeline as per Seurat in our supplementary section. **(2B)** Once the data-has been pre-processed, we further convert single cells to meta-cells, aggregated profiles of similar cells. **(3A)** We proceed to apply an LR filtering strategy to retain relevant intercellular features. **(3B)** These features are then scored via an interaction potential scoring function. **(4A)** In addition, we tailor the provided base GRN to each receiver cell type (RCT) so that we can **(4B)** score TF activity and calculate TF deltas. **(5)** using the calculated interaction potentials and TF activity, we fit a feature selection model to identify LR-TF edges. **(6)** We then use these LR-TF edge weights, along with the previously calculate TF deltas, to score LR activity. **(7)** Finally, we present a visualization layer for the user to explore the results from the analysis. (Created with BioRender.com and adapted from "Protein-Protein Interaction (PPI) Network", by BioRender.com (2024). Retrieved from https://app.biorender.com/biorender-templates)

2.2 – Cell to Cell communication methods

Next, we reviewed 36 state of the art scRNA-seq based cell-cell communication (CCC)[4,6,10–43] methods and compared them with *Decipher*, as summarized by their features in Table 1. We found methods either distinguish themselves through their biological use-cases or underlying methodologies. Fifteen of these methods embed intracellular components in their LR activity analysis (Supplementary Table ST.3). Among this subset, *Decipher* was most similar with four other methods: NicheNet, MultiNicheNet, CytoTalk and scMLNet (Supplementary Table ST.1). We excluded CytoTalk from our comparison as, unlike *Decipher*, NicheNet and MultiNicheNet, differential communication analysis was not embedded into their prioritization score but rather included in a subsequent comparison of output networks. We also excluded scMLnet as their output is a prioritized sub-network rather than a prioritization score. Furthermore, MultiNicheNet is a newer iteration of NicheNet that corrects for inter-sample effects. Both approaches are

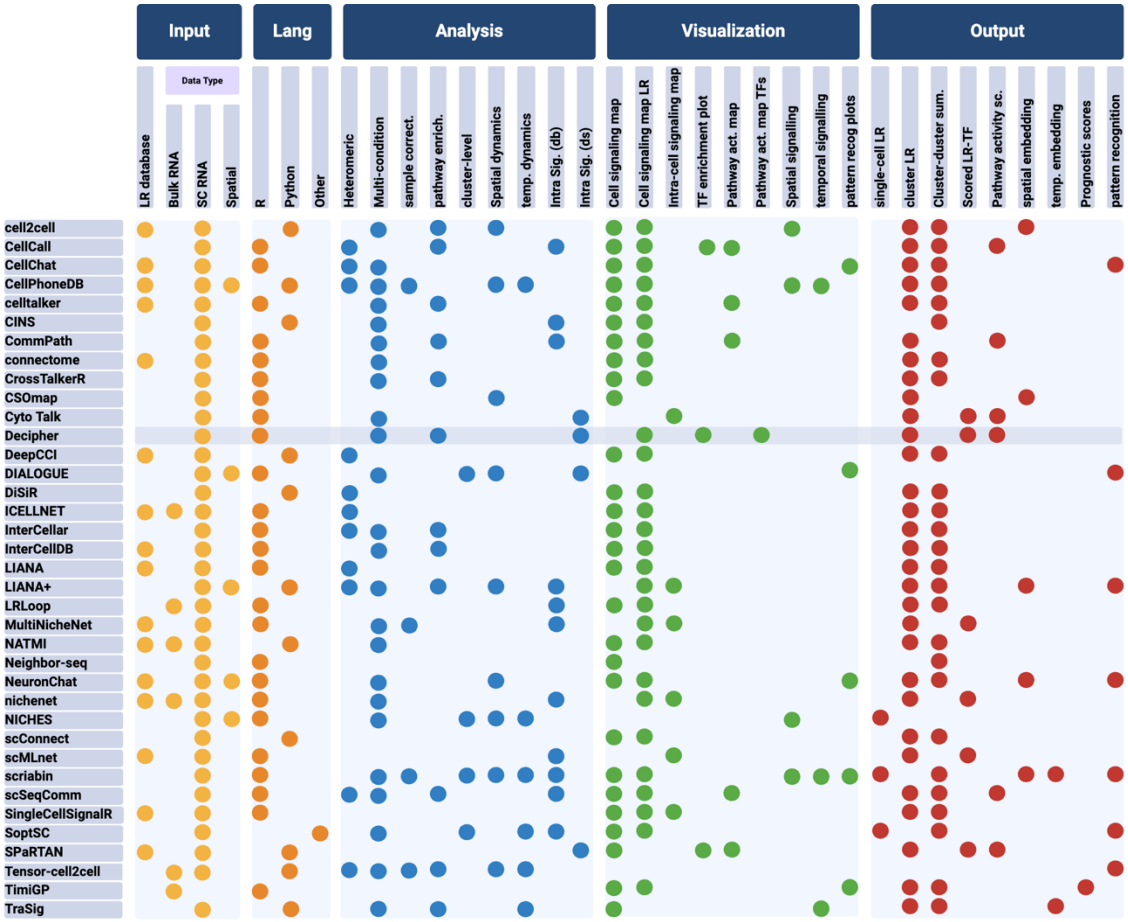

Table 1 – Comparison of CCC methods: The figure above compares 37 CCC methods across five categories: Input, language, analysis, visualization, and output. Additionally, the row corresponding to the *Decipher* method is further shaded for clarity. *Decipher* shows similarity to most methods in terms of input and language, where it focuses on scRNA-seq data and is written in R (25 out of 37, including *Decipher*). It differs, however, in its analysis, visualization and output. Analysis-wise, the main point of difference is its focus on intracellular signalling and, more specifically, doing so in a dataset driven manner. As shown in the table, most other methods that do intracellular signalling use a database-driven approach (11 out of 15). In terms of visualization, *Decipher* shares with most methods producing cell-cell signalling maps that embed LR pairs (28 out of 37, including *Decipher*). However, unlike most other methods , *Decipher* does not include visualizations that aggregate these interactions, as LR pairs scores are not given for specific SCTs (28 out of 37). Decipher, like CellCall, SPaRTAN, NicheNet and LIANA+ include plots that visualize intracellular signalling cascades from LR pairs to TFs. Unlike any other method, we include a compound plot that link LRs to TFs to pathway activity information. Finally, in terms of outputs, *Decipher* is like most other methods in produced LR activity scores at the cluster level (30 out of 37, including *Decipher*) and shares similarities with methods NicheNet, MultiNicheNet, CytoTalk, scMLNet, scSeqComm and SPARTAN in producing LR-TF scores. (Created with BioRender.com and adapted from "Multi-panel Table (Layout 5x3)", by BioRender.com (2024). Retrieved from https://app.biorender.com/biorender-templates)

151 summarized in their "general prioritization scheme", which we utilized in this study[33]. Furthermore, we
152 relied on NicheNet's latest prior-knowledge networks "NicheNet-v2".

153 For completeness we included one more intracellular CCC method, LIANA+[28], as well as two
154 popular CCC methods that do not embed intracellular responses but do calculate LR signalling activity:
155 Connectome[17] and NATMI[6].

156 2.3 Datasets

157 We performed eight case-control comparisons across six publicly available scRNA-seq datasets to assess
158 the performance of *Decipher* in diverse experimental settings (Table 2).

159 We studied immune responses of cord blood (CBMC) and peripheral blood mononuclear cells
160 (PBMC) to the viral mimic poly-IC (PIC)[44]. We studied immune responses to BCG vaccination in mice and the
161 Pfizer-BioNTech COVID-19 vaccine in humans. We also studied the autoimmune diseases Lupus and Sepsis
162 according to the datasets described in Table 2. Furthermore, we studied the response of breast cancer
163 patients to immune checkpoint blockade.

#	Species	Dataset and tissue type	Case	n	Cells	Control	n	Cells
1	Human	**Poly-IC stimulation** of cord blood (CBMC) and peripheral blood mononuclear cells (PBMC). (Read et al.[44])	Poly-IC treatment of PBMC	2	10,906	Unstimulated PBMC	2	11,564
2			Poly-IC treatment of CBMC	2	9,616	Unstimulated CBMC	2	10,016
3	Mice	**Immune response to BCG vaccination** in lung tissue from healthy and day 21 vaccinated mice (Lee et al.[45])	21 days post vaccination	5	7,000	Unvaccinated	5	21,000
4	Human	**immune response to the Pfizer-BioNTech COVID-19 mRNA vaccine** in PBMCs sampled from healthy volunteers at baseline and day 22 after primary dose/day 1 after secondary dose (Arunachalam et al.[46]).	1 day postsecondary mRNA vaccination	6	28,890	Unvaccinated	6	31,028
5	Human	**Systemic Lupus (SLE)** in PBMCs sampled from subjects exhibiting SLE and healthy volunteers (Perez et al.[47]).	SLE	26	113,204	No SLE	22	72,833
6	Human	**Sepsis** in PBMCs sampled from subjects in ICU with either sepsis or without sepsis (Reyes et al.[48])	ICU + Sepsis	8	8,948	ICU	7	8,505
7	Human	**Clonal expansion response of breast cancer patients to immune checkpoint blockade** in tumour biopsies taken from TNBC or ERP breast cancer patients before and after ICB treatment with anti-PD1. A subset of patients exhibited T cell expansion after treatment (Bassez et al.[49]).	TNBC before anti-PD1, expansion	5	23,624	TNBC before anti-PD1, no expansion	7	16,183
8			ERP before anti-PD1, clonal expansion	3	8,989	ERP before anti-PD1, no clonal expansion	12	30,299

Table 2 – summary of selected benchmarking datasets. Outline of the eight comparisons across six datasets with which we benchmarked various aspects of *Decipher*. For each, we present an index value, a brief description of the dataset and tissue type, the case and control conditions as well as the number of samples (n) and cells in each of these subsets. For further information refer to supplementary table ST.4 and to the methods section. (Created with BioRender.com)

164

165 2.4 – Predicting active ligand – receptor pairs in a system

166 To evaluate the capacity of *Decipher* to predict active ligand-receptor (LR) pairs in the condition of interest,
167 we compared Decipher with four state-of-the-art methods: LIANA+[28], NicheNet[33], Connectome[17] and
168 NATMI[6].

169 We assessed the ligand-receptor (LR) predictions for each method by evaluating (a.i) the number
170 of LR pairs reported, (a.ii) the number of reported LR pairs above one (σ), two (2σ), and three standard
171 deviations (3σ), (b) the degree of overlap between the top 100 LR pairs, (c.i) the Spearman correlation (ρ_s)
172 between these and, (c.ii) the depth of the search space to find the top 100 consensus LR pairs (i.e. each
173 consensus interaction has to be ranked below the reported search space size for the pair of methods), and
174 finally (d) ROC and AUC curves for comparison. Metrics (a) to (c) are evaluated entirely in – silico, whereas

(d) is based on experimentally determined singling pathways induced by a set of cytokines, chemokines and growth factors (Cytosig)[50]. Notably, the Cytosig database comprises only a subset of ligands (62 out of 829) from our reference LR database[6].

a

Index	comparison	Reported interactions					> 1 σ					> 2 σ					> 3 σ				
		D	L	N	C	T	D	L	N	C	T	D	L	N	C	T	D	L	N	C	T
1	PIC 5yr old	679	1821	5566	4166	4166	40	208	1024	390	681	20	73	108	166	5	9	36	0	76	0
2	PIC Cord	570	2302	6648	5088	5088	38	257	1179	497	1052	25	51	166	239	35	14	25	4	122	0
3	BCG	618	4335	11710	14947	14947	25	451	2246	1961	1869	10	148	214	830	114	6	38	0	312	6
4	COVID	683	2348	9659	12075	16899	41	380	1661	1318	2634	16	27	330	544	171	6	0	5	256	10
5	Lupus	158	467	1948	4147	3818	13	73	339	474	677	3	1	47	213	93	1	0	0	93	3
6	Sepsis	273	1147	5683	8476	8476	7	160	1006	1011	1739	3	15	159	406	200	3	0	2	183	7
7	TNBC	594	2142	8863	9960	9960	16	331	1548	1065	1714	8	59	125	460	161	5	8	0	218	11
8	ERP	466	2031	8119	9357	9357	11	342	1641	1082	1641	3	43	93	452	133	2	5	0	191	3

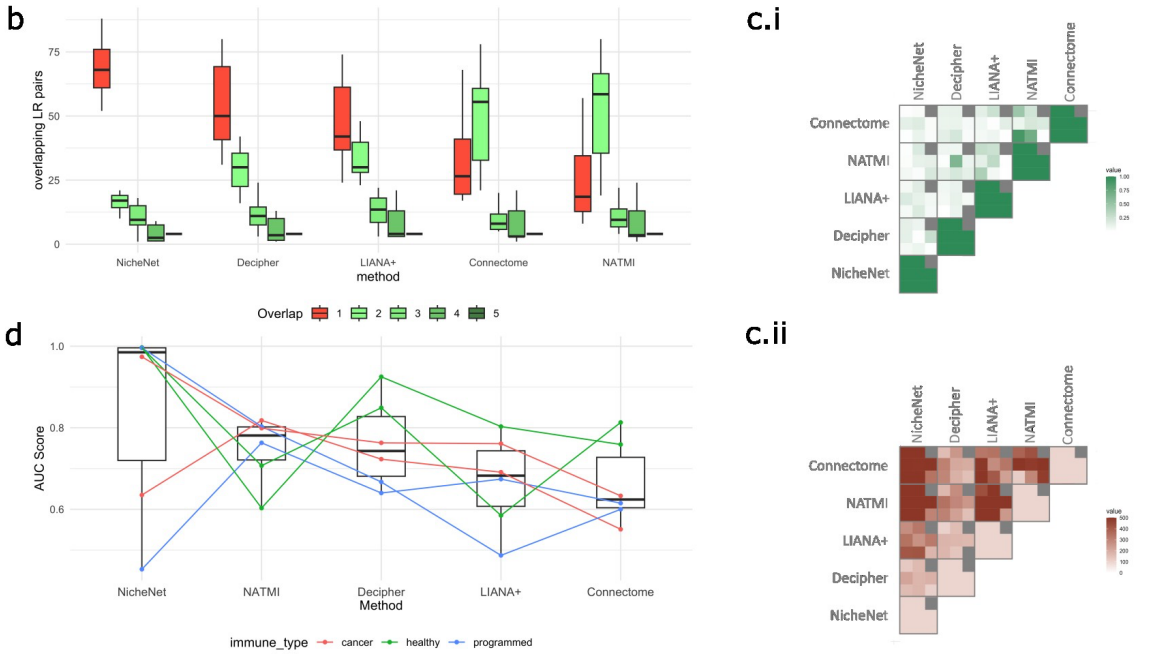

Figure 2. Comparison of performance in LR pairs prediction across five CCC methods. Comparison of outputs from Decipher (D), LIANA+ (L), NicheNet (N), Connectome (C) and NATMI (T). (a), Table summarizing reported interactions by each method across our eigh comparisons. We present both the total number of reported interactions, as well as the number of significant interactions at distinct thresholds defined by each method's prioritization scores' standard deviation. Decipher treats SCTs as a mixed cluster, most other methods score interactions for each SCT-RCT pair. Therefore, we selected the absolute maximum score for each interaction across all SCT-RCT pairs as representative of that interaction (for both reporting and further comparisons). (b), boxplots of overlap between the top 100 interactions in the system reported by each method across all comparisons. Overlap covers both unique LR pairs (red), as well as multi-way overlaps (shades of green). (c.i.), compound heatmap of the Spearman correlation between the rankings of the top 100 overlapping LR pairs, where green indicates stronger correlation. each sub-square within the larger squares represent results for a single comparison. greyed out sub-squares are used as visual fillers or when two methods did not share at least 100 overlapping LR pairs. (c.ii), heatmap of the search space size required to find 100 overlapping LR pairs that are both highly ranked. (d), boxplot of AUC scores benchmarking the performance of Decipher with the other frameworks. We report the AUC scores for each method's predictions using Cyosig scores to define true labels. Two of our datasets, 'Lupus' and 'Sepsis in ICU' are omitted from this last comparison, as Cytosig did not defined enough active ligands for meaningful use of ROCs. Other datasets are categorized as cancer, healthy (Poly-IC stimulation) and programmed (vaccination) and represented by superimposed points traced across all methods.

***Decipher* consistently reports less interactions than other methods.** As shown in Fig. 2a, across all eight comparisons, the total number of reported LR interactions, as well as LR pairs above 1σ, 2σ, and 3σ for *Decipher* was markedly lower than other methods. Interestingly, NicheNet did not report any LR

interactions above 3σ for most of the comparisons suggesting that their reported LR scores do not differ significantly from one another.

***Decipher* displayed similar overlap patterns to LIANA+.** As illustrated in Fig 2b, among the top 100 LR interactions for each comparison, most of the LR interactions reported by NicheNet (> 60) were not corroborated by any other method. As for two-way overlaps, there was strong consensus between Connectome and NATMI (> 50), suggesting a similar underlying structure (supported by upset plots shown in SF.2), and to a lesser extent for LIANA+ and *Decipher* (> 25). Notably, interactions for which there was consensus across all methods were found rarely (<5). Additionally, three-way, and four-way overlaps were also relatively uncommon (<10).

There is little agreement in LR rankings between methods. Heatmaps of Fig 2c (Spearman correlation and search-space) further indicated that the underlying analysis pipeline of each method differs significantly, favouring some LR pairs over others. A notable exception was the consensus between NATMI and Connectome, where two out of eight comparisons showed strong correlation $(\sim 0.89, \sim 0.70)$ (Fig. SF.3 BCG and ERP comparisons). Additionally, inspecting both the search space heatmap and the Spearman correlation suggested that even though *Decipher*, LIANA+, and NicheNet showed weak overall correlation between their top 100 consensus LR pairs, the size of the search space required to find overlapping pairs between Decipher and NicheNet $(\mu = 167)$, and Decipher and LIANA+ $(\mu = 157)$ was smaller than the other pairwise search-spaces $(\mu = 455)$. Together, this indicated that Decipher prioritized largely a similar set of LR interactions to NicheNet and LIANA+ but differed in their assigned ranking.

Comparative performance of *Decipher* with other top performing CCC methods. We employed Cytosig[50] to evaluate the capacity of the methods to recover experimentally determined signaling paths from single-cell profiles. We include NicheNet as a positive control, as their reference prior-knowledge network (NicheNet-v2) was partly constructed from Cytosig experiments[51]. Additionally, we excluded the Sepsis and Lupus data sets from this comparison because Cytosig did not identify enough active ligands in them to make meaningful comparisons (Fig. SF.5). As expected, the positive control, NicheNet, had the highest AUC performance. *Decipher* and NATMI had comparable central tendencies. On its favour, NATMI exhibited a tighter inter-quantile range, although *Decipher* displayed stronger performance in the upper quartile group (Fig. 2d, SF. 6). Overall, the data show that Decipher can recover known signaling paths with high accuracy whilst maintaining the flexibility to detect novel pathways.

2.5 – Accounting for intracellular responses through context-specific integrated LR/TF networks.

Predicting LR activity that drives downstream intracellular responses is critical for understanding disease processes. To evaluate this component of *Decipher*, we first assessed the degree of CT-context-specificity of iSNs by calculating Spearman correlation (ρ_S) on the weights of overlapping LR-TF interactions in different CTs for each comparison. We repeated this analysis on LR-TF interactions related to a subset of the top ten overlapping TFs. Lastly, we compared the consistency of *Decipher's* data-driven networks to NicheNet's prior-knowledge networks for the same system by reporting on general statistics of LR-TF edges inferred by each method. We compared *Decipher* and NicheNet over six datasets and eight comparisons, highlighted in Table 2. Unlike Section 2.4, we did not use Connectome and NATMI, as they do not model downstream responses. Similarly, we excluded LIANA+ from this analysis as it does not provide a quantitative score of the influence of LRs on downstream TFs.

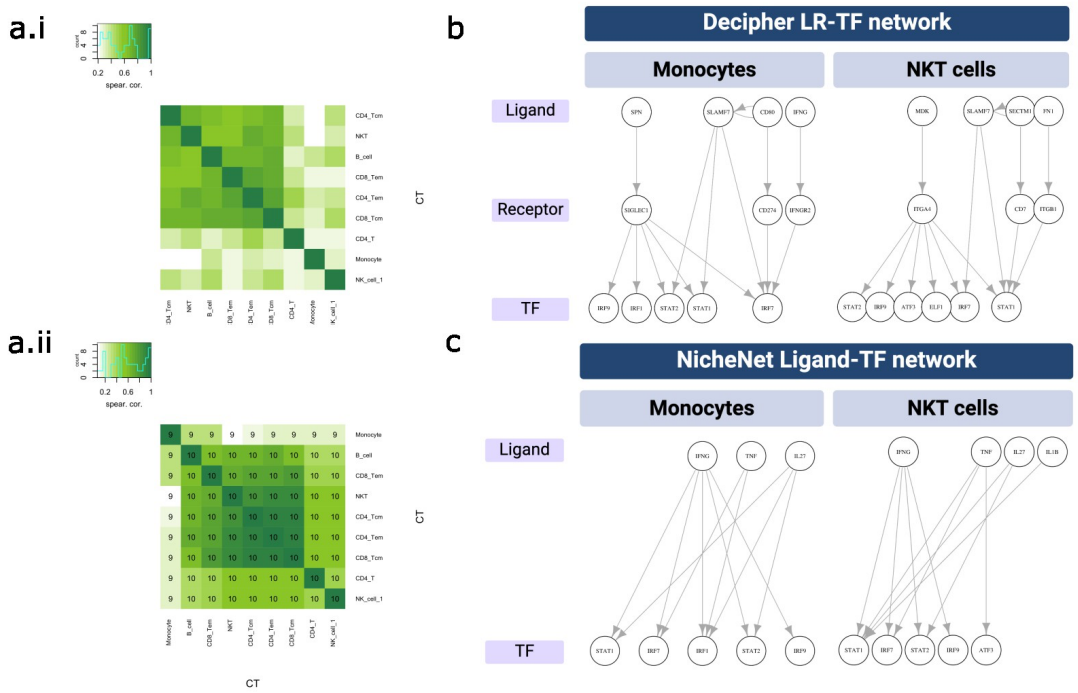

d

Index	comparison	cell type	Top positive Decipher				Top positive NicheNet				Top negative Decipher			
			LR	# TF		∩(D,N)	LR	# TF		∩(D,N)	LR	# TF		∩(D,N)
				D	N			D	N			D	N	
1	PIC 5yr old	Monocyte	SPN-SIGLEC1	66	21	1	IFNG-IFNGR2	26	84	8	ADAM15-ITGB1	8	14	0
2	PIC Cord	CD4_Tem	SECTM1-CD7	91	8	6	EBI3-IL6ST	2	10	0	SIRPB2-CD47	19	2	0
3	BCG	Memory CD4	CCL2-CCR5	100	34	5	CD48-CD2	4	12	0	CCL19-CCR7	85	28	0
4	pFizer mRNA	C8	C1QB-CD33	66	2	0	IFNG-IFNGR2	21	13	2	HGF-CD44	30	15	1
5	Sepsis	Mono MS3	THBS1-CD36	88	30	4	CD99-PILRA	80	5	0	APP-CD74	72	47	5
6	Lupus	Non-class Mono	MIF-CD74	96	21	5	HLA-C-LILRA3	49	17	2	THBS1-CD47	32	22	1
7	TNBC	T	LGALS3-LAG3	102	19	1	CD86-CD28	0	31	0	IL7-IL7R	103	30	5
8	ERP	T	LGALS3-LAG3	52	16	0	ICAM1-ITGAL	0	27	0	PIP-CD4	32	13	2

Figure 3. Comparison of intra-cellular signalling components. (a.i) Heatmap of Spearman correlation of LR-TF weights for each pair of CTs and their overlapping interactions for Poly-IC stimulated PBMCs. **(a.ii)** Heatmap of Spearman correlation of LR-TF pairs upstream of the top ten overlapping TFs across all CTs for Poly-IC stimulated PBMCs. Numbers indicate the number of said TFs present in any two-way comparison. **(b)** Graph representations of the top ten *Decipher* LR-TF edges for Monocyte and NKT CTs. **(c)** Graph representations of the top ten NicheNet LR-TF edges for Monocyte and NKT CTs in Poly-IC stimulated PBMCs. **(d)** Summary table of *Decipher* (D) and NicheNet (N) LR-TF relationships for *Decipher*'s top positive/negative LR pairs, as well as NicheNet's top positive LR pair. We report the number of TFs (#TF) downstream of the selected LR pairs, as well as their overlap (intersection D,N). For *Decipher*, we report on TFs whose LR-TF edge-weights are at least 5% of the largest weight for that interaction. For NicheNet, we report on all TFs directly connected to the selected ligands.

LR pairs impact on TFs in a context-specific manner. To assess the context-specificity of the produced iSNs we first calculated Spearman correlation on the *Decipher* weights of matching LR-TF relationships for different receiver cell types (RCTs) across all comparisons (Fig. 3a.i and SF.8). From this, we found low agreement between most iSNs, evidenced by the low correlation. We reasoned that this may partly reflect the LR filtering strategy and differences in intracellular responses, rather than actual bona fide differences in mechanistic relationships. To address this issue, for each comparison we selected a subset TF_o of the top ten overlapping TFs across all RCTs. For this subset, we once again performed Spearman correlation on the matching LR-TF relationships whose $TFs \subset TF_o$. We observed stronger correlation for the overlapping TF_o sub-networks (Fig. 3a.ii, SF.9) than for the general overlapped iSNs. We further

observed that while the iSNs of some CTs exhibited stronger similarity between them (e.g., CD4 Tcm and CD4 Tem in Fig 3a.ii), others did not (e.g. Monocytes and NK cells in Fig 3a.ii). Together, this suggests that the iSN networks built by *Decipher* differ between RCTs and are therefore context-specific.

We proceeded to focus on two CTs with distinct networks, Monocytes and NKT cells, from the Poly-IC stimulated PBMC dataset. For these we extracted the top ten LR-TF edges across the iSN and presented them as networks (Figure 3b). As shown, we observed no overlap between the edges across the two CTs, even though the networks shared the TFs IRF7, IRF9, STAT1 and STAT2. This further highlights the context-specificity of the effect of LR signals on downstream intracellular responses. Furthermore, we observed the presence of well-known ligands IFNG, CD80 and SLAMF7 in the Monocyte iSN and SLAMF7 in NKT cells.

There is little commonality between LR-TF relationships inferred by *Decipher* and NicheNet. We selected the same set of TFs as identified for the two CTs above and used NicheNet's Ligand-TF model to extract the top edges between NicheNet's top 10 CT-specific Ligands and said TFs (Fig 3c). Both these networks identified IFNG, TNF and IL27 as the main ligands regulating our TFs of interest. The IFNG-IRF7 relationship was the only relationship that was corroborated between *Decipher* and NicheNet.

Finally, for each of the eight comparisons, we extracted (a) the top-positive *Decipher* (b) the top-positive NicheNet and (c) the top-negative *Decipher* LR pairs for selected CTs. These LR pairs are needed by NicheNet to construct LR-TF sub-networks, as the method requires specifying ligands of interest. In Fig. 3d, we report on the number of TFs downstream of each of selected LR pair for *Decipher* and NicheNet, as well as on the overlap of said TFs. The lack of overlap between reported LR-TF relationships for *Decipher* and NicheNet illustrates that the analysis pipeline of each method differs significantly, favouring some LR-TF connections over others. We further present specific edges of said LR-TF relationships in Fig SF.10, showcasing that *Decipher* not only provides the strength of regulation, but also the mode of influence (activation/inhibition), whereas NicheNet focuses on relative influence (strength) without direction.

2.6 – Map system level cell – cell communication

Linking LR pair activity to downstream TF activation enables the elucidation of signals being received by a single RCT as well as their induced effects. LR signalling can be visualized across all CTs to obtain a global view of cellular communication in the condition of interest. To compare this aspect of *Decipher* to LIANA+ and NicheNet we performed a qualitative comparison of *Decipher's* default CCC visualisation as well as LIANA+ and NicheNet's analogous cell signalling maps for the CBMC response to Poly-IC. To make the results more comparable, we visualized the results from all three methods using the Decipher framework.

***Decipher* produces visualizations that are interpretable**. We found that *Decipher's* aggregation of SCTs into a mixed sender cluster implicitly summarizes information and therefore results in a more manageable and interpretable visualization as compared to methods that characterize LR signalling by SCT and RCT. To produce a *Decipher* map, such as the one seen in Fig 4, we relied on three metrics (i) relative abundance, (ii) differential expression, and (iii) *Decipher* scores. The first two metrics are calculated for both SCT ligands and RCT receptors. Within SCTs, these metrics help determine where ligands most likely originated. Analogously, in RCTs, these metrics allow comparison across CTs of the potential to receive said ligand. The *Decipher* score allows the user to focus on interactions *Decipher* deems significant as per its prior calculation of LR signalling activity.

We found analogous versions of this map in both LIANA+ and NicheNet (Fig SF.11 and SF.12). These versions use different metrics, though they convey similar information. NicheNet, on the one hand, utilizes (i) average expression, and (ii) differential expression of the ligand in the SCT(s) and the receptor in the RCT(s) together with (iii) NicheNet ranks. Similarly, LIANA+ employs (i) the p-value of differential expression of the ligand/receptor, and the LIANA+ (ii) interaction statistic score. While the aim of these visualizations

is similar, we see that methods that produce scores specific to each SCT-RCT combination require more complex visualizations (i.e. more panels) to convey similar information.

Finally, as the above-mentioned metrics are interchangeable, we converted NicheNet and LIANA+ results for the CBMC response to Poly-IC to *Decipher's* format and presented the results in Fig SF.13. Here, we showcased the utility of *Decipher's* simplified approach of SCT aggregation, as opposed to methods that focused their analysis on SCT-RCT pairs like NicheNet and LIANA+, which resulted in less cluttered visualizations. In summary, though Decipher presented less information because it calculated signalling from aggregated SCTs, this resulted in cleaner visualizations that still allow the user to identify which CT a ligand likely originated from.

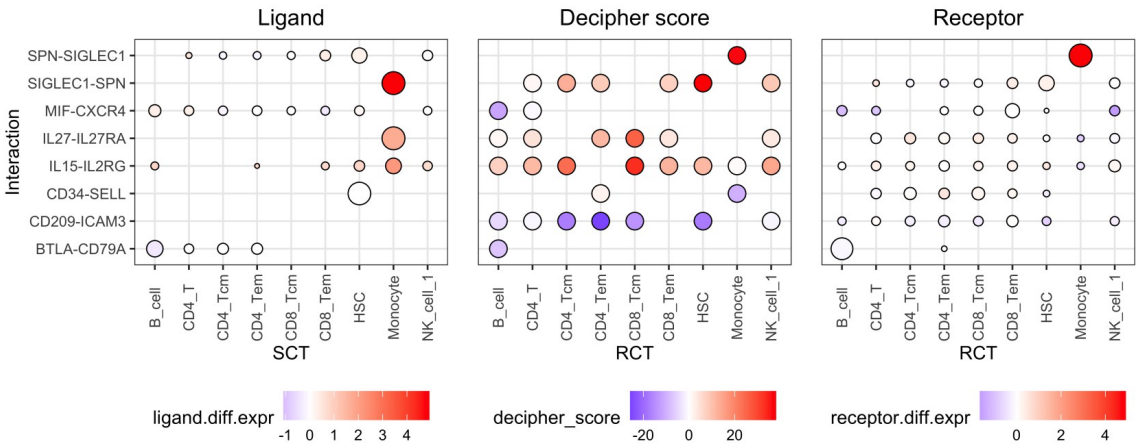

Figure 4. System-level signalling in the immune response of CMBC's to PIC. The Figure presents Decipher's system-level CCC visualization of LR signalling scores. The LHS sub-plot displays ligand-level statistics for the SCT and the RHS sub-plot presents receptor-statistics for the RCT. The size of the bubbles is indicative of the relative expression of the gene in the corresponding CT as compared to other CTs, whereas the colour indicates the differential expression of that same protein in case vs control for that same CT. The central sub-plot presents Decipher scores for all RCTs. Here, blue indicates a LR pairs is predicted to be inhibited, and red activated.

2.7 – Extracting mechanistic insights from *Decipher's* predictions

To assess the capacity of *Decipher* to extract mechanistic insights and candidate therapeutic targets from single-cell profiles, we focused on the single-cell experiment investigating immune responses to the Pfizer-BioNTech COVID-19 vaccine in humans[46]. This system was found to exhibit strong activation of the innate immune system and the emergence of a novel monocyte sub-population post-secondary vaccination; of particular interest to our testing, the intracellular activity of the monocyte sub-population was further characterized, and the system response was associatively linked to the ligand IFNG. Together, this presented a rich opportunity to contextualize this sub-population using *Decipher*, as well as to compare findings at distinct levels of biological regulation. With this dataset, we specifically aimed to identify the upstream signals that drive the activation this novel monocyte sub-population ($CD14^{+}BDCA1^{+}$PD-L1/C8) as it was identified by the authors to be a key component of the programmed immune response after vaccination.

We first assessed the intracellular signature across all CTs through our Δ_{TF} metric, which we subsequently compared to those reported by the original study (Fig. 5a). Next, we looked at the signalling patterns between top-ranked ligands and RCTs (Fig 5b). Additionally, we determined the likely origin of these top-ranked ligands, for which we used the same feature statistics leveraged for our system-level

305 visualization (Fig 5c). We produced a CCC map for the top 10 LR pairs signalling to the C8 cluster (Fig 5d), as
306 well as mapped the connections between these pairs and downstream TFs (Fig 5e).

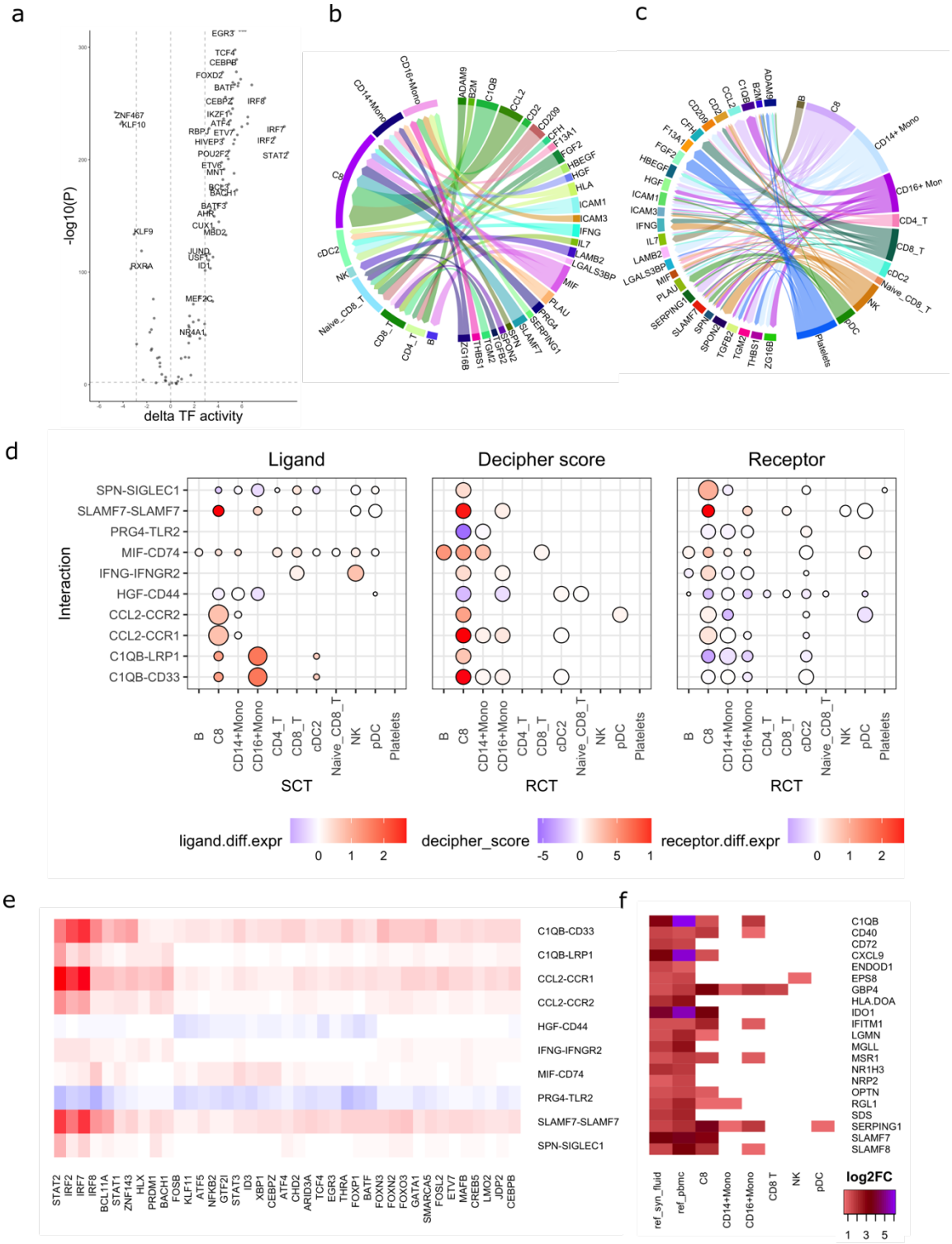

Figure 5. Mechanistic Insights in the Pfizer-BioNTech COVID-19 vaccine comparison. (a) Volcano plot of TF deltas in the C8 cluster. **(b)** Circos plot of top ligands signalling into RCTs (sized by Decipher score). **(c)** Circos plot of ligand production by all SCTs (sized by relative expression). **(d)** Multi-panel plot of global dynamics from the top 10 identified LR pairs in the C8 cluster (based on absolute Decipher scores). **(e)** Heatmap of individual LR-TF decipher scores for the top 10 LR pairs highlighted above. **(f)** Heatmap of reference log-FC of SLAMF7-high gene signature of synovial fluid (ref_syn_fluid) and PBMCs (ref_pbmc) from sorted CD14+ Monocytes from Simmons et al[52] plotted alongside differential expression profiles from three Monocyte populations (C8, CD14+ and CD16+), as well as CD8 T, NK and pDC cells.

The C8 cluster exhibited strong upregulation in interferon-related TFs. We identified a broad TF response in the C8 cluster (Fig. 5a, SF. 7). The C8 cluster displayed strong upregulation in subsets of the IRF and STAT family of TFs (IRF2, IRF7, IRF8, STAT1, STAT2), which play a major role in regulating the expression of interferon stimulated genes. This was in correspondence with previous findings, though previously reported down-regulation of the JUND and ATF3 TFs[46] was not substantiated by the *Decipher* analysis. Together, this suggests mixed agreement with originally reported findings, highlighting differences in methods.

Signalling primarily affected the innate immune compartment. We focused on global signalling patterns and found that signalling primarily affected the innate immune compartment, specifically the C8 cluster (Fig 5b.) We found well-known ligands among the prioritized LR interactions, including IL7, HLA, IFNG and SLAMF7. We investigated the origin of identified ligands and found that they were produced by a multitude of CTs (Fig 5c). A significant portion of these appear to be produced by $CD14^+$/$CD16^+$ Monocytes and C8 cells, suggesting crosstalk amongst innate immune cells. IFNG, a ligand-of-interest highlighted by the original authors, appears to be primarily produced by CD8 T and NK cells.

We found IFNG, SLAMF7, C1QB and CCL2 signalling into the C8 cluster. We further focused on the top 10 LR pairs for the C8 cluster (Fig 5d), where we more clearly saw the presence of IFNG. Additionally, we found stronger signalling into the C8 cluster through SLAMF7, CCL2 and C1QB pathways. SLAMF7 is produced by a multitude of CTs, particularly C8, NK cells, CD8 T cells and plasmacytoid dendritic cells (pDCs). CCL2 is primarily produced by C8s and is suggestive of autocrine signalling. C1QB, on the other hand, is produced in $CD16^+$ Monocytes and less so in C8 and cDC2 cells. Additionally, we identified two LR pairs, PRG4-TLR2 and HGF-CD44, that appear to be downregulated after vaccination. We mapped the most differentially active TFs downstream of C8's top LR pairs (Fig 5e) and found C1QB, CCL2 and SLAMF7 activation are strongly related to STAT2, IRF2, IRF7 and IRF8 activity, as well as moderately related to a much broader TF response. IFNG, SPN and HGF, on the other hand, have a more exclusive response.

We obtained further confirmation of SLAMF7 signalling in C8 by leveraging a previously published signature of $SLAMF7^{high}$ macrophages from synovial fluid and PBMCs[52]. We found that cluster C8, and to a lesser degree $CD16^+$ Monocytes, matched the reference signatures (Fig 5f). Though pDC, NK cells and CD8 T cells produce SLAMF7, these are neither identified by *Decipher* as receiving SLAMF7-SLAMF7 signalling, nor is such signalling apparent from the signature. This example suggests that though a CT may exhibit expression of both the cognate ligand and receptor, *Decipher* appropriately distinguishes expression from activity. Therefore, *Decipher* presents a wealth of insights at distinct regulatory layers, as well as system, cellular and molecular levels, which align with prior-findings as well as introduce novel hypotheses.

3 Discussion

Decoding the cellular and molecular events that drive disease processes and cellular responses to therapies requires the development of new methods that can extract deep mechanistic insights from single-cell profiles. Towards this goal, we developed *Decipher*, a novel computational pipeline that builds integrated cell signaling networks from single-cell profiles and unveils key cellular and molecular events that drive biological responses. We benchmarked *Decipher* against other state-of-the-art methods, and we showed that *Decipher* produces a manageable set of prioritized molecular pathways, can recover known signaling pathways with high accuracy and maintains the flexibility to detect novel pathways. Additionally, the data-driven approach employed by *Decipher* generates results that are cell-type and context-specific. Together, these three factors are crucial to unlocking the key cellular and molecular mechanisms that drive a biological system's response to perturbations and/or disease processes and bridges a current gap that exists with existing methods. *Decipher* also produces global cell-to-cell signaling maps that are easy to interpret in comparison to other methods, such as NicheNet and LIANA+. Finally, *Decipher* was able to recover the mechanism that drives a novel monocyte population enriched with interferon stimulated genes

that is markedly increased in frequency following secondary immunization with the Pfizer-BioNTech COVID-19 mRNA vaccine. Our findings demonstrate the utility of *Decipher* to decode biological processes in the form of ligand-receptor mediated TF-target gene networks and, in doing so, unveils novel therapeutic targets for experimental validation and clinical development, such as the role of pDC, CD8 T cells and NK cells and the IFNG/SLAMF7 axis in the response to COVID-19 vaccination and ensuing disease severity. Notably, there is a growing understanding that leveraging genetic evidence or single cell RNA-Seq profiles to prioritize therapeutic targets for drug development can markedly reduce failure rates[53,54] , and accordingly the unbiased mechanistic approach employed by Decipher is uniquely placed to inform the identification and prioritization of novel therapeutic targets.

Over 36 computational tools have been developed to interrogate cell-to-cell communication. However, the majority of these methods do not consider or model the downstream effects of ligand-receptor signalling. We reasoned that embedding intracellular networks would not be trivial, as methods that use data alone do not possess sufficient predictive power for network inference[55], while methods that rely only on prior knowledge naturally cannot detect novel pathways. We addressed this issue by developing *Decipher* to be capable to employ both prior knowledge and data-driven approaches to strike a balance between novelty and accuracy. We benchmarked *Decipher* against other state-of-the-art methods across diverse experimental settings and found that *Decipher* identified a focused set of LR scores across all data sets, evaluated as the reporting of a manageable set of interactions above $1\sigma, 2\sigma$, and 3σ. Interestingly, NicheNet and Connectome generated results with low dispersion, making it challenging to prioritize pathways for experimental validation studies. Of the top 100 LR interactions, we found little consensus across methods, as demonstrated by the low overlap and lack of correlation between the rankings. A notable exception was the moderate/strong overlap observed between Connectome and NATMI for all datasets excluding the Lupus and mRNA vaccine datasets, as well as the moderate overlap between *Decipher* and LIANA+ for, curiously, the Lupus and mRNA vaccine datasets. Additionally, we observed moderate correlation between *Decipher* and NATMI in the PBMC response to Poly-IC and for NATMI and Connectome in the BCG, Sepsis and ERP datasets. Our consensus heatmap, indicative of the size of the search space required to find similarly prioritized interactions, suggested some agreement in prioritization across all datasets between *Decipher* and NicheNet and *Decipher* and LIANA+. Together, we surmise from these observations that there is a lack of consensus across CCC inference methods, something previously highlighted by Dimitrov et al. and attributed to the diversity of scoring systems.[27] Despite such discrepancies, we could still observe similarities among methods that either embed intracellular signalling (e.g. *Decipher*, LIANA+ and NicheNet) or only look at the intercellular component (e.g. NATMI and Connectome).

We further evaluated the performance of these CCC methods against experimentally determined signaling pathways from Cytosig, a predictive model of cytokine activity trained on transcriptomic profiles of cytokine-treated systems. *Decipher* had strong performance in these analyses, with a median AUC of 0.75 and a range between ~ 0.65 and ~ 0.90. Overall, *Decipher* outperformed LIANA+ and Connectome and had comparable performance to NATMI. NicheNet, which we considered a positive control, was most aligned to Cytosig predictions. Although NicheNet had been shown to exhibit strong performance in benchmarking studies[33], it is important to note that NicheNet employs a knowledge graph approach to connect ligands and receptors to downstream gene regulatory networks. A limitation of the knowledge graph approach is that the data are generally not context-specific or cell type specific, and novel connections cannot be identified. One caveat to our benchmarking studies with Cytosig is that only 62 ligands are evaluated through this approach, which constitutes a small subset of the ligands used in our model. Furthermore, we excluded AUC results for Sepsis and Lupus from this comparison as Cytosig did not identify enough active ligands for meaningful analysis.

We proceeded to evaluate *Decipher's* iSNs, the underlying network connecting LR activity and intracellular responses. Here we compared *Decipher* with NicheNet alone, as the other selected methods either did not embed intracellular signalling (and therefore had no iSNs) or did not provide the required outputs for comparison. We found that the *Decipher's* iSN incorporated key information unaccounted for by NicheNet, namely the mode of influence of an interaction (activation/inhibition), which is calculated by linking LR and TFs in a data-driven way. Having the mode of influence of an interaction is useful, as it helps understand how to modulate the system of interest. We further showed that Decipher produces context-specific iSNs by calculating the correlation between edge-weights corresponding to distinct RCTs. We also calculated edge-weight correlations for sub-sampled iSNs, so as to compare networks related to the top ten overlapping TFs across each dataset. We found differences in the structure of iSNs of each RCT in all datasets. Additionally, for some datasets, we found clusters of more similar iSNs, for example the CD4 Tcm, CD4 Tem and CD8 Tcm cluster in the PBMC stimulated with Poly-IC, and the CD4 T and CD8 T cluster in the Lupus dataset (SF. 9). We extracted a sample subnetwork of the iSNs corresponding to Monocytes and NKT cells in the Poly-IC stimulated PBMCs and found that the results from NicheNet were restricted to well characterized immune pathways (IFNG, TNF, IL27 and IL1B) whereas *Decipher* identified a combination of pathways that were well-known (IFNG, SLAMF7, CD80) and some novel pathways (SPN, MDK, SECTIM1, FN1). Together, these findings demonstrate that *Decipher* provides deep insights into biological responses, including the mode/direction of regulatory effects, cell type specific regulatory networks, and can recover both known and novel pathways.

The individual cellular and molecular components modelled by *Decipher* do not exist in isolation but rather function as an integrated system. Accordingly, we aggregated our results into a global signalling map reflecting system-level communication. We compared visualizations that included both cellular-level information (which CTs were communicating with one another) and molecular-level information (what LR pairs were being used to transmit these messages). To do so, we looked at *Decipher's* visualization, as well as that of NicheNet and LIANA+'s. Here, we found a fundamental difference rooted on the differing approach to scoring LR pairs, where the latter methods calculate LR signalling between pairs of CTs, whereas *Decipher* aggregates all sender CTs into a single mixed cluster. While the explicit SCT-RCT approach reduces the need for the user to make a judgement about where a signal is coming from, it does result in visualizations that present significantly more elements, which is directly related to the number of SCTs. *Decipher*, on the other hand, produces visualizations with less elements due to the mixing of SCTs. Additionally, we do provide enough information for the user to infer likely SCTs for a ligand in a LR pair of interest. Therefore, compared to programs including NicheNet and LIANA+, *Decipher's* cell-cell signalling maps better addresses the problem of difficult-to-visualize cell-cell signalling maps.

To evaluate the capacity of *Decipher* to extract mechanistic insights from single-cell profiles, we focused on the immune response to the Pfizer-BioNTech COVID-19 mRNA vaccine. In their study, Arunachalam et al. found that a novel population of monocytes ($CD14^+BDCA1^+PD\text{-}L1^+$/C8 population) was markedly increased in frequency following secondary vaccination. The authors showed that the C8 population was characterized by Type I interferon response, TLR and inflammation, as well as displayed an increase in Interferon and STAT TFs and decrease in AP-1 TFs[46]. We employed *Decipher* to deconstruct the underlying mechanism at three distinct layers (LR signalling, LR-TF relationships and cell-to-cell signalling). We found stronger activation of the innate immune system, reflected in multiple LR pairs with strong *Decipher* scores for C8, $CD14^+$ and $CD16^+$ Monocytes (as opposed to few for other CTs). Additionally, we confirmed the previously reported upregulation of IFN and STAT family of TFs, showing upregulation of IRF2, IRF7, IRF8, STAT1, STAT2 and STAT3. Additionally, we observed upregulation of CEBPB, XBP1 and CUX1 and downregulation of KLF9, KLF10, BHLHE40 and EGR1 TFs in the C8 cluster as compared to $CD14^+$ Monocytes. Importantly, we found a significant amount of autocrine signalling in C8 cells, a phenomenon

446 generally observed in CCC[56], as well as cross-talk between innate immune CTs CD16$^+$ Monocytes, C8 cells
447 and cDC2 cells.

448 We confirmed previous data demonstrating that IFNG is a driver of the C8 population[46], as well as
449 identified CD8 T and NK cells as the primary producers of IFNG[57]. IFNG, however, was not the strongest
450 signal found by Decipher, as we also found significant signalling through the SLAMF7, CCL2 and C1QB ligands
451 into the C8 cluster. Notably, SLAMF7 is a self-ligand receptor from the signaling lymphocytic activation
452 molecule (SLAM) family and a potent regulator of interferon responses[58] and inflammatory macrophage
453 activation[59]. Importantly, IFNG and SLAMF7 have been previously implicated as a driver of a super-activated
454 macrophage state present in autoimmune diseases and severe COVID-19[52]. This state was reproduced in-
455 vitro through a two-step activation process which entailed initial IFNG priming of resting macrophages to
456 upregulate expression of SLAMF7 and interferon-induced genes, followed by engagement of SLAMF7 with
457 an activating antibody or recombinant SLAMF7 protein ligand, resulting in a highly proinflammatory state.[52].
458 Our data suggests that a similar mechanism drives the C8 population in response to secondary Pfizer-
459 BioNTech vaccination. Given that SLAMF7 is a self-ligand receptor, it is difficult to differentiate between the
460 ligand and receptor function of the same molecule based on mRNA data alone. To address this issue, we
461 examined the expression of a SLAMF7 activation signature in the data, and we showed that the C8
462 population strongly expressed the SLAMF7 activation signature, whereas CD8 T cells, NK cells, and
463 plasmacytoid dendritic cells expressed SLAMF7 but not the SLAMF7 activation signature. These data suggest
464 that CD8 T cells, NK cells and pDC are producing the ligand to signal to the C8 population and are not
465 responding to the ligand themselves. Moreover, the prolonged activation of the IFNG/SLAMF7 axis is a
466 logical therapeutic target for severe autoimmune diseases and infectious diseases[52], highlighting the
467 capacity of Decipher to identify targets for the development of new medicines.

468 *Decipher* has limitations that should be acknowledged. We observed intracellular activity to be
469 imbalanced, such as in our finding that some CTs have a greater number of differentially activated TFs. This
470 may impact the *Decipher* scores as they are linearly related to intracellular activity (Δ_{TF}) by our scoring
471 function. While it may be reasonable to give higher scores to interactions affecting CTs with greater
472 intracellular changes, this may need to be further addressed. A potential alternative could be to perform
473 absolute scaling on TF activity, so that $\Delta_{TF} \in [-1,1]$, and introduce a normalization factor
474 $\sum_{TF \in TFs} w_{LR-TF}$, such as in scSeqComm in which TF activity $\in [0,1]$ and the sum of a-priori association
475 scores for the TFs of a particular pathway is used as a normalization factor[37]. Furthermore, we noticed that
476 TF activity was highly correlated within each CT. This is not unexpected, as multi-collinearity/redundancy is
477 a known property of biological networks. However, multi-collinearity in the context of our LR-TF analysis
478 does pose a problem, as LR pairs that are most predictive of a TF's activity are likely to be selected for other
479 TFs. Here, we suggest implementing new scoring strategies for TF activity, something that is in active
480 development by the bioinformatics community. Conceptually, *Decipher* currently does not take into
481 account the fact that signaling occurs within local niches. This issue can be addressed by extending *Decipher*
482 to spatial transcriptomics data. Finally, we recognize that *Decipher* also does not consider feedback control
483 or response dynamics, and this can be included by extending Decipher to model dynamical systems
484 behaviour.

485 To conclude, we present *Decipher* as a modular pipeline for extracting mechanistic insights from
486 single-cell profiles through the integrated analysis of cell-to-cell communication and downstream signaling
487 events. *Decipher* (i) quantifies active LR pairs, (ii) accounts for downstream intracellular responses, (iii) maps
488 cell-cell communication to a systems level, and (iv) is capable of decoding biological responses in the form
489 of ligand-receptor mediated TF-target gene networks. We believe that *Decipher* will be invaluable as a tool
490 to accelerate the identification of novel therapeutic targets for human diseases, as well as accelerate the
491 development of new medicines.

4 Methods

4.1 *Decipher* – a pipeline to build and score Integrated Signalling Networks (iSNs)

Collection and processing of single-cell transcriptomic data of poly-IC stimulation to human blood mononuclear cells from Read et al.[44] Processed single-cell data was directly obtained from the original authors. We used the original cell-type labels, so no further pre-processing was required. Alternatively, the data is available from Gene Expression Omnibus (Accession Number GSE184383).

Collection and processing of mouse single-cell transcriptomic data of lung-tissue response to BCG vaccination from Lee Et al.[45] Count data was downloaded from Gene Expression Omnibus (Accession Number: GSE244126). No cell-type labels were provided, so we used sctype[60] along with two reference tissue profiles (Immune system and lung) to assign two cell-type labels to each cluster, retaining the label with the largest score for each cluster.

Collection and processing of human single-cell transcriptomic data of human PBMC response to Pfizer-BioNtech vaccination from Arunachalam Et al.[46] Count data and phenotypic data were downloaded from Gene Expression Omnibus (Accession Number: GSE171964). We used the original cell-type labels, so no further pre-processing was required.

Collection and processing of single-cell transcriptomic data of PBMCs from subjects with Systemic Lupus (SLE) and healthy control from Perez et al.[47] Count data, including phenotypic data, was downloaded from Gene Expression Omnibus (Accession number: GSE174188). We used the original cell type labels, so no further pre-processing was required. We constrained our analysis to the subset of samples belonging to female samples of Asian ancestry that were either classified as healthy or as 'managed' SLE cases.

Collection and processing of single-cell transcriptomic data of PBMCS from ICU patients with/without sepsis from Reyes et al.[48] Count data with phenotypic information were downloaded from the Broad institute Single-cell Portal (Accession Number: SCP548). We used the original cell-type labels, so no further pre-processing was required.

Collection and processing of single-cell transcriptomic data of PBMCS from breast cancer patients treated with immune checkpoint blockade from Bassez et al.[49] Processed single-cell data was downloaded directly from Diether Lambrecht's laboratory website, through their Data portal. We used the original cell type labels, so no further pre-processing was required.

Pre-processing pipeline. If needed, a standard pre-processing pipeline based on Seurat[61] is delineated in "Supplementary Note 3: Pre-processing pipeline for single-cell profiles". Said pipeline addresses standard scRNA-seq pre-processing, beginning after the raw data has been read aligned to produce gene counts $\boldsymbol{D}$. In brief, this pre-processing pipeline covers the filtering out poor quality, invalid or damaged cells, normalization of gene counts, using these counts to produce clusters $\mathbb{G}_j$ of similar cells and determining representative genes for each cluster for downstream cell-labelling. To aid with interpretability of results, we recommend clusters are labelled using expert judgement. If expert judgement is not available, there are several cell-type labelling tools, one of which we used (sc-type[60]) to pre-process lung-tissue data from Lee et al[45].

Notation. We include a reference notation table in Supplementary Note 2: "Decipher Notation Table". If required, this table is a useful accompaniment to the following sections.

Generate meta cells for each cluster. To remove noise and account for zero-inflation of gene counts in scRNA-seq data, we applied the method proposed by PISCES[62]. Here, individual single-cell profiles were aggregated into meta cells by adding the counts of each gene across individual cells. To do so, we first had to determine which cells were most like one another and therefore could be pooled together. In line with this, and so as to preserve biological differences, we performed meta-cell aggregation for each cluster $\mathbb{G}_j$ separately. Additionally, we generated meta-cells for the case $\mathbb{G}_j^c$ and control $\mathbb{G}_j^t$ subsets individually.

Firstly, we determined two parameters: the number of cells per meta-cell, k, and the number of meta-cells for the subsets $\{\mathbb{G}_j^c, \mathbb{G}_j^t\}$, $m_{\mathbb{G}_j}$. The first parameter, k, controls the density of the meta-cell gene counts, as the more cells in a meta-cell, the less likely it is to exhibit zero-inflation. The second parameter, $m_{\mathbb{G}_j}$, serves two purposes: preventing the overlap of cells between meta-cells and producing enough meta-cells for our downstream modelling. To determine the parameter k, we visually inspected the distribution of the sum of gene counts for each cell in each group $\{\mathbb{G}_j^c, \mathbb{G}_j^t\}$, a proxy of the sparseness of the data, and iteratively tested k parameter values until we raised the median value of all distributions above a range of 7,500 to 10,000 counts. We determined the parameter $m_{\mathbb{G}_j}$, such that on average no cell appeared in more than one meta-cell, and further constrained this value such that both subsets have the same number of meta-cells.

With these, we proceeded to determine which cells are most like each other, and therefore can be aggregated into meta-cells. To do so, we first calculated a distance matrix $\boldsymbol{E}_{\mathbb{G}_j^c}$ between all cells in subset $\mathbb{G}_j^c$. Given two cells from $\mathbb{G}_j^c$, represented by their gene counts as columns of $\boldsymbol{D}_{\mathbb{G}_j^c}$, say $\boldsymbol{x}_i$ and $\boldsymbol{x}_k$ for the ith and k^{th} cells respectively, the Euclidean distance between these two cells is calculated as follows.

$$d(x_i, x_k) = \sqrt{\sum_{n=1}^{N} \left(x_{i,n} - x_{k,n}\right)^2}$$

Where N is the total number of genes and $x_{i,n}$ and $x_{k,n}$ are the counts of gene n for cells i and k, respectively. The same procedure was repeated for the control subset $\mathbb{G}_j^t$, yielding $\boldsymbol{E}_{\mathbb{G}_j^t}$.

Next, for each case cluster $\mathbb{G}_j^c$, we randomly selected $m_{\mathbb{G}_j}$ cells. For each selected cell C_a, we determined its k nearest neighbours $\mathcal{S}_a = \{C_{a,1}, C_{a,2}, \cdots, C_{a,k}\}$ using the Euclidean distance matrix $\boldsymbol{E}_{\mathbb{G}_j^c}$. Note that the top k closest neighbours of C_a does include C_a as well ($C_a \in \mathcal{S}_a$).

We produced meta-cells by summing the gene-counts of the k nearest neighbours to those of the base cell, calculated as

$$\boldsymbol{D}_{C_a}^m = \boldsymbol{D}_{C_{a,1}} + \boldsymbol{D}_{C_{a,2}} + \cdots + \boldsymbol{D}_{C_{a,k}}$$

Finally, each meta-cell was normalized by its new library size and scaled by a factor of 10^6 for interpretability, yielding the meta-cell expression matrix $\boldsymbol{D}_{\mathbb{G}_j^c}^m$. Said process was repeated for the control subset, giving $\boldsymbol{D}_{\mathbb{G}_j^t}^m$. Naturally, we combine these matrices to produce cluster-specific meta-cell expression matrices $\boldsymbol{D}_{\mathbb{G}_j}^m$, as well as a case-specific meta-cell matrix $\boldsymbol{D}_c^m$, a control-specific meta-cell matrix $\boldsymbol{D}_t^m$, and a dataset wide meta-cell matrix $\boldsymbol{D}^m$.

Calculate an interaction potential matrix for each cluster. Like most CCC methods, we relied on gene co-expression to determine potential LR pair signalling between clusters. However, unlike other methods, we distinguish between LR pairs that have the potential to signal and LR pairs that are actively modulating a system's response and note that the former is a requirement for the latter.

To calculate the interaction potential between clusters we relied on a reference LR interaction network represented by a directed, unweighted graph $\mathcal{G}_{LR}(\mathcal{N}_{LR}, \mathcal{E}_{LR})$, such that the nodes $(\mathcal{N}_{LR})$ represent ligands and receptors, whereas an edge $(\mathcal{E}_{LR})$ only originates from the ligand to the receptor if there is evidence of complementarity between the two.

Collection of reference LR pair database. We used the reference LR graph from the ConnectomeDB2020 database, as provided by NATMI[6]. We chose ConnectomeDB2020 because LR interactions presented within the database were manually curated, based on literature support and focused on monomeric interactions, i.e. a single ligand interacts with a single receptor. This aligned with our current version of the pipeline, as *Decipher* currently does not support multimeric interactions.

Structural filters of ligands and receptors. Ligands L were retained if they were expressed in at least 10% of cells in any of the case-control subsets $\{\mathbb{G}_j^c, \mathbb{G}_j^t\}$ of any one cluster $\mathbb{G}_j$. We addressed ligands at a global level because we assumed that ligand-concentration in the environment is the driver of signalling, as opposed to ligand production by a single cluster.

Receptors, on the other hand, were filtered on a cluster-by-cluster basis. For each cluster $\mathbb{G}_j$, receptors $R_{\mathbb{G}_j}$ were only retained if they were expressed in at least 10% of the cells of either the case or the control blocks of that cluster i.e., $\{\mathbb{G}_j^c, \mathbb{G}_j^t\}$**.** Receptors were treated as cluster-specific because receptor signalling is biologically constrained to individual cells.

For each cluster $\mathbb{G}_j$, we use the selected ligands L and receptors $R_{\mathbb{G}_j}$ to filter the set of considered LR pairs in $\mathcal{G}_{LR}(\mathcal{N}_{LR}, \mathcal{E}_{LR})$, yielding a reduced list of potential cluster-specific LR pairs $\mathrm{P}_{\mathbb{G}_j}$ that we used for downstream analysis.

Calculating interaction potential for all cluster-specific LR pairs. Next, we quantified the interaction potential between ligand-receptor pairs $\mathrm{P}_{\mathbb{G}_j}$ for each meta-cell of the case subset $\mathbb{G}_j^c$. Given a receiving meta-cell from $\mathbb{G}_j^c$, represented by its gene counts as a column of $\boldsymbol{D}_{\mathbb{G}_j^c}^m$, say $\boldsymbol{x}_i^m$ for the ith meta-cell, as well as a ligand l and receptor r corresponding to an LR pair in $\mathrm{P}_{\mathbb{G}_j}$, the interaction potential i for this LR pair in this meta-cell is defined as:

$$i = \sqrt{\overline{l^c} \times x_{i,r}^m}$$

Where $x_{i,r}^m$ corresponds to the counts of receptor r for meta-cell i and $\overline{l^c}$ to the mean-ligand expression of ligand l in $\boldsymbol{D}_{\boldsymbol{c}}^m$. Extending this analysis to all LR pairs in all meta-cells in $\mathbb{G}_j^c$, we obtain an interaction potential matrix $\mathbf{I}_{\mathrm{P}_{\mathbb{G}_j}}^c$. In a similar manner, we obtain an equivalent matrix for the control cluster $\mathbf{I}_{\mathrm{P}_{\mathbb{G}_j}}^t$**.** Giving us a combined interaction potential matrix $\mathbf{I}_{\mathrm{P}_{\mathbb{G}_j}}$ for cluster $\mathbb{G}_j$**.**

Functional filtering of LR pairs. We further filtered LR pairs in $\mathbf{I}_{\mathrm{P}_{\mathbb{G}_j}}$ to retain only those interactions that exhibited significant differential expression between the case and control subsets. Here, we used Seurat's *FindMarkers* function which implements differentially expressed genes between clusters using the Wilcoxon Rank Sum test. We retained LR pairs that exhibited an adjusted p-value lesser than 0.01 and a $\log_2(\cdot)$ fold-change greater than 0.1. Here, we assumed that the interaction potential had to exhibit some change across the case and control subsets to be relevant for downstream analysis.

Selecting LR pairs that exhibit low correlation. We found a significant portion of LR pairs in our interaction potential matrix $\mathbf{I}_{\mathrm{P}_{\mathbb{G}_j}}$ exhibited high correlation between each other, and thus could affect downstream statistical modelling. We investigated and saw that highly correlated LR pairs occurred primarily when multiple ligands shared a single receptor (Figure **SF15.**)

To address this, we split each set of LR pairs $\mathrm{P}_{\mathbb{G}_j}$ into one-to-one $(1 \rightarrow 1)$ and many-to-one $(N \rightarrow 1)$ interactions, where the former indicate receptors with only on complementary ligand, and the later receptors with multiple complementary ligands, i.e. $\mathrm{P}_{\mathbb{G}_j} = \left\{\mathrm{P}_{\mathbb{G}_j}^{1\rightarrow 1} \cup \mathrm{P}_{\mathbb{G}_j}^{N\rightarrow 1}\right\}$.

Given the lower correlation between one-to-one interactions $(1 \rightarrow 1)$, we retained all of $\mathrm{P}_{\mathbb{G}_j}^{1\rightarrow 1}$.

For $\mathrm{P}_{\mathbb{G}_j}^{N\rightarrow 1}$ LR interactions, we selected representative features such that we retained both captured biological variance while reducing correlation among features. To determine which interactions are most like each other, and therefore can be clustered together, we first calculated a distance matrix between the $\mathrm{P}_{\mathbb{G}_j}^{N\rightarrow 1}$ interactions for each cluster $\mathbb{G}_j$. Given two interactions from $\mathbb{G}_j$, represented by their interaction potential as rows of $\mathbf{I}_{\mathrm{P}_{\mathbb{G}_j}}$, say $\mathbf{i}_a$ and $\mathbf{i}_b$ for the ath and b^{th} row, respectively. The distance between these two interactions is calculated as follows:

$$d(\mathbf{i}_a, \mathbf{i}_b) = 1 - \rho_S(\mathbf{i}_a, \mathbf{i}_b)$$

Where $\rho_S(\cdot)$ represents the Spearman correlation function. Repeating this process for all pairs of interactions from $\mathrm{P}_{\mathbb{G}_j}^{N\rightarrow 1}$, we obtained a distance matrix $\mathbf{H}_{\mathrm{P}_{\mathbb{G}_j}^{N\rightarrow 1}}$ between the $(N \rightarrow 1)$ interactions in $\mathbb{G}_j$.

We proceeded to use hierarchical clustering on this distance matrix $\mathbf{H}_{\mathbb{P}_{\mathbb{G}_j}^{N\rightarrow 1}}$ to define interaction clusters $\mathbb{H}_j$. As the subsets produced by hierarchical clustering are defined using a distance metric threshold, we set this parameter such that we had approximately the same number of unique receptors as in the $\mathrm{P}_{\mathbb{G}_j}^{N\rightarrow 1}$ subset. We proceeded to randomly select one representative LR interaction from each subset, giving us a down-sampled set $\mathbb{P}_{\mathbb{G}_j}^{N\rightarrow 1}$. Lastly, we retained the set of LR interactions $\mathbb{P}_{\mathbb{G}_j} = \left\{\mathrm{P}_{\mathbb{G}_j}^{1\rightarrow 1} \cup \mathbb{P}_{\mathbb{G}_j}^{N\rightarrow 1}\right\}$. We retained the LR pairs $\mathbb{P}_{\mathbb{G}_j}$ from the previously calculated interaction matrices $\left\{\mathbf{I}_{\mathrm{P}_{\mathbb{G}_j}}^{c}, \mathbf{I}_{\mathrm{P}_{\mathbb{G}_j}}^{t}\right\}$ to give us sets of representative interaction potential matrices $\{\mathbf{I}_{\mathbb{G}_j}^{c,h}, \mathbf{I}_{\mathbb{G}_j}^{t,h}\}$ for each cluster $\mathbb{G}_j$.

Build context-specific GRNs for each cluster. we proceeded to build cluster-specific gene regulatory networks (GRNs). To do so, we relied on benchmarked base GRNs provided by *CellOracle*[7] (CO), as well as their tailoring pipeline. GRNs are networks $\mathcal{G}_{GRN}(\mathcal{N}_{GRN}, \mathcal{E}_{GRN})$, such that the nodes $(\mathcal{N}_{GRN})$ represent TFs and TGs, whereas an edge $(\mathcal{E}_{GRN})$, represents the directed regulatory relationships between TFs and TGs. The sub-network $\mathcal{G}_{reg}(\mathcal{N}_{reg}, \mathcal{E}_{reg})$, whose nodes $(\mathcal{N}_{reg})$ comprise of a source TF and its TGs and edges $(\mathcal{E}_{reg})$ a directed regulatory relationship between the source TF and its TGs, is also known as a regulon. From now on, we use the term TF and regulon interchangeably, as for our intent and purposes their definition is the same.

Collection of reference GRN. We selected CO as their GRNs are generated using scATAC-seq data which, unlike computationally derived GRNs, ensures there is biological evidence of a TF-TG relationships.

Tailoring of reference GRN using CellOracle and filters. Given CO's requirement for python objects and difficulties with mapping Seurat objects to the required format, for each cluster $\mathbb{G}_j$ we re-

processed our count data using the scanpy[63] pipeline. Here, we first removed genes with no counts. Next, we normalized cell counts by their library size. We then filtered these normalized counts to retain the top 3000 most variable genes, which we re-normalized by their new library size. We took the natural logarithm of these re-normalized counts, and scaled them unit variance and zero mean, giving us $\boldsymbol{D}^{s,3000}_{\mathbb{G}_j}$.

We ran the CO pipeline on $\boldsymbol{D}^{s,3000}_{\mathbb{G}_j}$, producing directed, weighted and signed GRNs. We found that the tailored GRNs produced by CO were very dense (i.e. they had many edges). Therefore, to reduce some of this density, we retained the strongest 20,000 edges in the network (based on the absolute value of their weights). This first pruning was a more global, entire-network based-pruning. We complemented this global pruning with a more local pruning of edges, such that for each TF present in the network, we restricted its outdegree to a maximum of 40, retaining the largest edges within each sub-network. We denote this network as $(\vec{B}_{\mathbb{G}_j})$.

We performed pruning of the network to increase the heterogeneity of regulons (as large regulons naturally tended to have overlap with smaller regulons). Given increased regulon heterogeneity, we expected TF activity scores to be less correlated among each other. Furthermore, selecting the top 3000 variable genes during *scanpy* pre-processing naturally constrains our GRN to only those 3000 genes.

Score cluster-specific regulon activity. Using $\vec{B}_{\mathbb{G}_j}$, we proceeded to use regulons $\mathcal{R}$ to determine the activation of individual TF based upon the expressions of their TGs.

We employed elements of PAGODA2[64] to determine the activity for all TF(s) in $\vec{B}_{\mathbb{G}_j}$. For each cluster $\mathbb{G}_j$, we fed the representative matrix $\boldsymbol{D}^{m}_{\mathbb{G}_j}$ into PAGODA2's 'mixture model' to derive a residual matrix $\boldsymbol{\mathcal{P}}_{\mathbb{G}_j}$, capturing the over- or under-dispersion of each gene in each meta-cell. Thereafter, for each TF $\mathbb{f}$, we subset the rows of the residual matrix $\boldsymbol{\mathcal{P}}_{\mathbb{G}_j}$ to restrict it to the TG(s) $\mathcal{S}_{\mathbb{f}}$ related to the TF in question., $\boldsymbol{\mathcal{P}}_{\mathbb{G}_j,\mathcal{S}_{\mathbb{f}}}$.

We applied PAGODA2's function *testPathwayOverdispersion()* which in turn applies the implicitly restarted Lanczos bidiagonalization algorithm to $\boldsymbol{\mathcal{P}}_{\mathbb{G}_j,\mathcal{S}_{\mathbb{f}}}$ to obtain its largest singular value and singular vector. These cell-specific vectors from the residual matrix $\boldsymbol{\mathcal{P}}_{\mathbb{G}_j,\mathcal{S}_{\mathbb{f}}}$ were aligned to the largest singular vector derived above. The resulting matrix, $\boldsymbol{F}_{\mathbb{G}_j,\mathcal{S}_{\mathbb{f}}}$ represents the TF activity scores for TF $\mathbb{f}$ in cluster $\mathbb{G}_j$.

Lastly, we concatenated the TF activity scores $\boldsymbol{F}_{\mathbb{G}_j,\mathcal{S}_{\mathbb{f}}}$ for all TF(s) in the cluster $\mathbb{G}_{\boldsymbol{j}}$ to attain a regulon activity score matrix $\boldsymbol{F}_{\mathbb{G}_j}$ representing the entire cluster $\mathbb{G}_{\boldsymbol{j}}$.

Build an integrated signalling network (iSN) for each cluster. To understand the propagation of signalling from LR pairs to GRNs, we built integrated signalling networks (iSN). iSNs implicitly connect LR interaction networks and GRNs. Given that the wiring and activation of these networks is context-dependent, we constructed iSNs for each cluster $\mathbb{G}_{\boldsymbol{j}}$. To connect these two, we inferred edges between LR pairs and TFs by modelling the relationship between the variables representing them. Here, we used interaction potential scores $\mathbf{I}^{h}_{\mathbb{G}_j}$ for LR pairs and the regulon activity scores $\boldsymbol{F}_{\mathbb{G}_j}$ for TFs. Both matrices $\left\{\mathbf{I}^{h}_{\mathbb{G}_j}, \boldsymbol{F}_{\mathbb{G}_j}\right\}$ present scores at the meta-cell level.

We split the problem into $\hat{n}$ problems, one for each TF in $\boldsymbol{F}_{\mathbb{G}_j}$. Given a TF $\mathbb{f}$, represented by the TF activity across all meta-cells in $\mathbb{G}_j$, i.e. a row in $\boldsymbol{F}_{\mathbb{G}_j}$, we its relationship with all LR pairs relevant to cluster$\mathbb{G}_j$, i.e. $\mathbf{I}^h_{\mathbb{G}_j}$. We modelled this problem as

$$\boldsymbol{F}_{\mathbb{G}_j}(\mathbb{f}) \approx R\left(\mathbf{I}^h_{\mathbb{G}_j}\right)$$

Where R represents our regression function. Specifically, we used a Random Forest (RF) regressor. [] While our regressor does produce a function R, we leverage the feature selection component of the model rather than the predictive capabilities. Thereby, we shift focus to the 'importance' metric, which we use as weights of the directed edges in our iSN.

Furthermore, biologically, LR pairs either activate or suppress TF activity. Therefore, we calculated a proxy of mode of influence for each LR-TF relationship. Given an interaction from $\mathbb{G}_j$, represented by its interaction potential as a row of $\mathbf{I}^h_{\mathbb{G}_j}$, say $\mathbf{i}_a$ for the ath row, and a given TF $\mathbb{f}$, represented by its activity score as rows in $\boldsymbol{F}_{\mathbb{G}_j}$, we incorporate the mode of influence of $\mathbf{i}_a$ on $\mathbb{f}$ as

$$sgn\big(\rho_S(\mathbb{f}, \mathbf{i}_a)\big)$$

Where $\rho_S(\cdot)$ represents the Spearman correlation function. Therefore, given the importance $imp(\mathbf{i}_a, \mathbb{f})$calculated from our random Forest R for the relationship between these two, we define the weight of the edge connecting said nodes as

$$imp(\mathbf{i}_a, \mathbb{f}) * sgn\big(\rho_S(\mathbb{f}, \mathbf{i}_a)\big)$$

Repeated across $\hat{n}$ problems yields a weighted adjacency matrix $\boldsymbol{A}$ representing the weights of all new edges between all LR interactions in $\mathbf{I}^h_{\mathbb{G}_j}$ and all TF(s) in $\boldsymbol{F}_{\mathbb{G}_j}$.

Using this adjacency matrix to represent edges between LR pairs and TFs, the resulting iSN is a directed and weighted graph $\mathcal{G}_{iSN}(\mathcal{N}_{iSN}, \mathcal{E}_{iSN})$, such that the nodes $\mathcal{N}_{iSN}$ represent LR pairs and TFs, whereas edges $(\mathcal{E}_{iSN})$ represent the observed relationship between the two. Naturally, it is possible to extend this network so as to include TGs, as this information is already encoded for in the tailored, cluster-specific GRN $\vec{B}_{\mathbb{G}_j}$.

Score interactions for each cluster. Having obtained cluster-specific signed, weighted, and directed iSNs $\mathcal{G}_{iSN}(\mathcal{N}_{iSN}, \mathcal{E}_{iSN})$ comprising of ligands, receptors, TF(s) and TG(s), we utilized these networks to score LR interactions for each cluster $\left(\mathbb{G}_j\right)$.

Since biologically we are comparing the case under investigation with a control, we quantified differences in the ith LR interaction within a cluster $\mathbb{G}_j$, between the two conditions, denoted as $\left(\theta_{\mathbb{G}_j,i}\right)$. To do so, we first calculated the changes in intracellular TF activity in each cluster.

Evaluate differential expression of regulons across different conditions in each cluster. We proceeded to calculate the changes in intracellular activity, i.e. the changes in TF activity $\boldsymbol{F}_{\mathbb{G}_j}$ across the case and control conditions to then propagate this change using the iSN and thus determine LR pairs responsible for the observed signalling.

Given a TF $\mathbb{f}$ in cluster $\mathbb{G}_j$, whose activity in the case condition $\boldsymbol{f}^c_{\mathbb{G}_j,\mathbb{f}}$ and in the control condition $\boldsymbol{f}^t_{\mathbb{G}_j,\mathbb{f}}$ are represented by rows in $\boldsymbol{F}_{\mathbb{G}^c_j}$ and $\boldsymbol{F}_{\mathbb{G}^t_j}$, respectively, the differential expression of said TF, denoted here as $\boldsymbol{\Delta}_{\mathbb{G}_j,\mathbb{f}}$ is defined as

$$\boldsymbol{\Delta}_{\mathbb{G}_j,\mathbb{f}} = \widehat{\boldsymbol{f}^c_{\mathbb{G}_j,\mathbb{f}}} - \widehat{\boldsymbol{f}^t_{\mathbb{G}_j,\mathbb{f}}}$$

Where $\widehat{\boldsymbol{f}^{c}_{\mathbb{G}_j,\mathscr{f}}}$ and $\widehat{\boldsymbol{f}^{t}_{\mathbb{G}_j,\mathscr{f}}}$ represent the median activity of TF $\mathscr{f}$ in the case and control conditions of cluster $\mathbb{G}_j$, respectively. Extending the same for all TFs gives us a vector of delta scores $\boldsymbol{\Delta}_{\mathbb{G}_j}$ for cluster $\mathbb{G}_j$.

Calculate the Decipher score. To calculate $\theta_{\mathbb{G}_j,i}$ we aggregated (i) the activating/suppressing weights obtained from the adjacency matrix ($\boldsymbol{A}$) of our iSN, as well as (ii) changes observed in the TF activity $\left(\boldsymbol{\Delta}_{\mathbb{G}_j}\right)$ while comparing the case under investigation with the control.

Assuming, that a given i^{th} LR interaction within a cluster $\mathbb{G}_j$, with shown to be connected to $k: 1 \rightarrow K$ TF(s) in our iSN, the generic equation comes to be:

$$\theta_{j,i} = \sum_{k=1}^{K} \left(\boldsymbol{A}_{[i,k]} \cdot \boldsymbol{\Delta}_{\mathbb{G}_j,k} \right)$$

Henceforth, for any given LR interaction, we refer to the above scores as the '***decipher score***' for that particular LR interaction. Extend this to all interactions relevant to cluster $\mathbb{G}_j$, we obtain the cluster-wide *Decipher* scores $\boldsymbol{\theta}_{\mathbb{G}_j}$.

Taken altogether, with this approach, we achieve our two primary aims of building cluster-specific Integrated Signalling Networks and scoring interaction activity based on such a network.

References

1. Armingol, E., Officer, A., Harismendy, O. & Lewis, N. E. Deciphering cell–cell interactions and communication from gene expression. *Nat Rev Genet* (2020) doi:10.1038/s41576-020-00292-x.

2. Baysoy, A., Bai, Z., Satija, R. & Fan, R. The technological landscape and applications of single-cell multi-omics. *Nature Reviews Molecular Cell Biology* vol. 24 695–713 Preprint at https://doi.org/10.1038/s41580-023-00615-w (2023).

3. Ramilowski, J. A. *et al.* A draft network of ligand–receptor-mediated multicellular signalling in human. *Nat Commun* **6**, 7866 (2015).

4. Jin, S. *et al.* Inference and analysis of cell-cell communication using CellChat. *Nat Commun* **12**, (2021).

5. Almet, A. A., Cang, Z., Jin, S. & Nie, Q. The landscape of cell–cell communication through single-cell transcriptomics. *Current Opinion in Systems Biology* vol. 26 12–23 Preprint at https://doi.org/10.1016/j.coisb.2021.03.007 (2021).

6. Hou, R., Denisenko, E., Ong, H. T., Ramilowski, J. A. & Forrest, A. R. R. Predicting cell-to-cell communication networks using NATMI. *Nat Commun* **11**, (2020).

7. Kamimoto, K. *et al.* Dissecting cell identity via network inference and in silico gene perturbation. *Nature* **614**, 742–751 (2023).

8. Baran, Y. *et al.* MetaCell: Analysis of single-cell RNA-seq data using K-nn graph partitions. *Genome Biol* **20**, (2019).

807 9. Fan, J. *et al.* Characterizing transcriptional heterogeneity through pathway and gene set
808 overdispersion analysis. *Nat Methods* **13**, 241–244 (2016).

809 10. Cheng, J., Zhang, J., Wu, Z. & Sun, X. Inferring microenvironmental regulation of gene
810 expression from single-cell RNA sequencing data using scMLnet with an application to
811 COVID-19. *Brief Bioinform* **22**, 988–1005 (2021).

812 11. Armingol, E. *et al.* Inferring a spatial code of cell-cell interactions across a whole animal
813 body. *PLoS Comput Biol* **18**, (2022).

814 12. Zhang, Y. *et al.* CellCall: Integrating paired ligand-receptor and transcription factor
815 activities for cell-cell communication. *Nucleic Acids Res* **49**, 8520–8534 (2021).

816 13. Garcia-Alonso, L. *et al.* Single-cell roadmap of human gonadal development. *Nature* **607**,
817 540–547 (2022).

818 14. Cillo, A. R. *et al.* Immune Landscape of Viral- and Carcinogen-Driven Head and Neck
819 Cancer. *Immunity* **52**, 183-199.e9 (2020).

820 15. Yuan, Y. *et al.* CINS: Cell Interaction Network inference from Single cell expression data.
821 *PLoS Comput Biol* **18**, (2022).

822 16. Lu, H. *et al.* CommPath: An R package for inference and analysis of pathway-mediated
823 cell-cell communication chain from single-cell transcriptomics. *Comput Struct Biotechnol*
824 *J* **20**, 5978–5983 (2022).

825 17. Raredon, M. S. B. *et al.* Computation and visualization of cell–cell signaling topologies in
826 single-cell systems data using Connectome. *Sci Rep* **12**, (2022).

827 18. Nagai, J. S., Leimkühler, N. B., Schaub, M. T., Schneider, R. K. & Costa, I. G. CrossTalkeR:
828 analysis and visualization of ligand-receptorne tworks. *Bioinformatics* **37**, 4263–4265
829 (2021).

830 19. Ren, X. *et al.* Reconstruction of cell spatial organization from single-cell RNA sequencing
831 data based on ligand-receptor mediated self-assembly. *Cell Res* **30**, 763–778 (2020).

832 20. Hu, Y., Peng, T., Gao, L. & Tan, K. CytoTalk: De novo construction of signal transduction
833 networks using single-cell transcriptomic data. *Sci. Adv* **7**, (2021).

834 21. Yang, W. *et al.* DeepCCI: a deep learning framework for identifying cell–cell interactions
835 from single-cell RNA sequencing data. *Bioinformatics* **39**, (2023).

836 22. Jerby-Arnon, L. & Regev, A. DIALOGUE maps multicellular programs in tissue from
837 single-cell or spatial transcriptomics data. *Nat Biotechnol* **40**, 1467–1477 (2022).

838 23. Vahid, M. R. *et al.* DiSiR: Fast and robust method to identify ligand-receptor interactions
839 at subunit level from single-cell RNA-sequencing data. *NAR Genom Bioinform* **5**, (2023).

840 24. Noël, F. *et al.* Dissection of intercellular communication using the transcriptome-based
841 framework ICELLNET. *Nat Commun* **12**, (2021).

842 25. Interlandi, M., Kerl, K. & Dugas, M. InterCellar enables interactive analysis and
843 exploration of cell–cell communication in single-cell transcriptomic data. *Commun Biol*
844 **5**, (2022).

845 26. Jin, Z. *et al.* InterCellDB: A User-Defined Database for Inferring Intercellular Networks.
846 *Advanced Science* **9**, (2022).

847 27. Dimitrov, D. *et al.* Comparison of methods and resources for cell-cell communication
848 inference from single-cell RNA-Seq data. *Nat Commun* **13**, (2022).

849 28. Dimitrov, D. *et al.* LIANA+: an all-in-one cell-cell communication framework.
850 doi:10.1101/2023.08.19.553863.

851 29. Xin, Y. *et al.* LRLoop: a method to predict feedback loops in cell–cell communication.
852 *Oxford Bioinformatics* **38**, 4117–4126 (2022).

853 30. Browaeys, R. *et al.* MultiNicheNet: a flexible framework for differential cell-cell
854 communication analysis from multi-sample multi-condition single-cell transcriptomics
855 data. doi:10.1101/2023.06.13.544751.

856 31. Ghaddar, B. & De, S. Reconstructing physical cell interaction networks from single-cell
857 data using Neighbor-seq. *Nucleic Acids Res* **50**, (2022).

858 32. Zhao, W., Johnston, K. G., Ren, H., Xu, X. & Nie, Q. Inferring neuron-neuron
859 communications from single-cell transcriptomics through NeuronChat. *Nat Commun* **14**,
860 (2023).

861 33. Browaeys, R., Saelens, W. & Saeys, Y. NicheNet: modeling intercellular communication
862 by linking ligands to target genes. *Nat Methods* **17**, 159–162 (2020).

863 34. Raredon, M. S. B. *et al.* Comprehensive visualization of cell-cell interactions in single-cell
864 and spatial transcriptomics with NICHES. *Bioinformatics* **39**, (2023).

865 35. Jakobsson, J. E. T., Spjuth, O. & Lagerström, M. C. scConnect: a method for exploratory
866 analysis of cell-cell communication based on single-cell RNA-sequencing data.
867 *Bioinformatics* **37**, 3501–3508 (2021).

868 36. Wilk, A. J., Shalek, A. K., Holmes, S. & Blish, C. A. Comparative analysis of cell–cell
869 communication at single-cell resolution. *Nat Biotechnol* (2023) doi:10.1038/s41587-
870 023-01782-z.

871 37. Baruzzo, G., Cesaro, G. & Camillo, B. Di. Identify, quantify and characterize cellular
872 communication from single-cell RNA sequencing data with scSeqComm.
873 *BIOINFORMATICS* **38**, 1920–1929 (2022).

874 38. Cabello-Aguilar, S. *et al.* SingleCellSignalR: Inference of intercellular networks from
875 single-cell transcriptomics. *Nucleic Acids Res* **48**, (2021).

876 39. Wang, S., Karikomi, M., Maclean, A. L. & Nie, Q. Cell lineage and communication network
877 inference via optimization for single-cell transcriptomics. *Nucleic Acids Res* **47**, (2019).

878 40. Ma, X. *et al.* SPaRTAN, a computational framework for linking cell-surface receptors to
879 transcriptional regulators. *Nucleic Acids Res* **49**, 9633–9647 (2021).

880 41. Armingol, E. *et al.* Context-aware deconvolution of cell–cell communication with Tensor-
881 cell2cell. *Nat Commun* **13**, (2022).

882 42. Li, C. *et al.* TimiGP: Inferring cell-cell interactions and prognostic associations in the
883 tumor immune microenvironment through gene pairs. *Cell Rep Med* **4**, (2023).

884 43. Li, D. *et al.* TraSig: inferring cell-cell interactions from pseudotime ordering of scRNA-
885 Seq data. *Genome Biol* **23**, (2022).

886 44. Read, J. F. *et al.* Lipopolysaccharide-induced interferon response networks at birth are
887 predictive of severe viral lower respiratory infections in the first year of life. *Front*
888 *Immunol* **13**, (2022).

889 45. Lee, A. *et al.* BCG vaccination stimulates integrated organ immunity by feedback of the
890 adaptive immune response to imprint prolonged innate antiviral resistance. *Nat*
891 *Immunol* (2023) doi:10.1038/s41590-023-01700-0.

892 46. Arunachalam, P. S. *et al.* Systems vaccinology of the BNT162b2 mRNA vaccine in humans.
893 *Nature* **596**, 410–416 (2021).

894 47. Perez, R. K. *et al.* Single-cell RNA-seq reveals cell type-specific molecular and genetic
895 associations to lupus. *Science (1979)* **376**, (2022).

896 48. Reyes, M. *et al.* An immune-cell signature of bacterial sepsis. *Nature Medicine* vol. 26
897 333–340 Preprint at https://doi.org/10.1038/s41591-020-0752-4 (2020).

898 49. Bassez, A. *et al.* A single-cell map of intratumoral changes during anti-PD1 treatment of
899 patients with breast cancer. *Nat Med* **27**, 820–832 (2021).

900 50. Jiang, P. *et al.* Systematic investigation of cytokine signaling activity at the tissue and
901 single-cell levels. *Nat Methods* **18**, 1181–1191 (2021).

902 51. Browaeys, R. Evaluation of NicheNet's ligand-target predictions.
903 https://github.com/saeyslab/nichenetr/blob/master/vignettes/model_evaluation.md.

904 52. Simmons, D. P. *et al. SLAMF7 Engagement Superactivates Macrophages in Acute and*
905 *Chronic Inflammation , Accelerating Medicines Partnership (AMP) RA/SLE Network †,*
906 *Deepak A. Sci. Immunol* vol. 7 https://www.science.org (2022).

907 53. Dann, E. *et al.* Single-cell RNA sequencing of human tissue supports successful drug
908 targets. doi:10.1101/2024.04.04.24305313.

909 54. Minikel, E. V., Painter, J. L., Dong, C. C. & Nelson, M. R. Refining the impact of genetic
910 evidence on clinical success. *Nature* (2024) doi:10.1038/s41586-024-07316-0.

911 55. Petri, T., Altmann, S., Geistlinger, L., Zimmer, R. & Küffner, R. Addressing false discoveries
912 in network inference. *Bioinformatics* **31**, 2836–2843 (2015).

913 56. Ramilowski, J. A. *et al.* A draft network of ligand-receptor-mediated multicellular
914 signalling in human. *Nat Commun* **6**, (2015).

915 57. Li, C. *et al.* Mechanisms of innate and adaptive immunity to the Pfizer-BioNTech
916 BNT162b2 vaccine. *Nat Immunol* **23**, 543–555 (2022).

917 58. O'Connell, P. *et al.* SLAMF7 Is a Critical Negative Regulator of IFN-α–Mediated CXCL10
918 Production in Chronic HIV Infection. *The Journal of Immunology* **202**, 228–238 (2019).

59. Simmons, D. P. *et al. SLAMF7 Engagement Superactivates Macrophages in Acute and Chronic Inflammation , Accelerating Medicines Partnership (AMP) RA/SLE Network †, Deepak A. Sci. Immunol* vol. 7 https://www.science.org (2022).

60. Ianevski, A., Giri, A. K. & Aittokallio, T. Fully-automated and ultra-fast cell-type identification using specific marker combinations from single-cell transcriptomic data. *Nat Commun* **13**, (2022).

61. Hao, Y. *et al.* Integrated analysis of multimodal single-cell data. *Cell* **184**, 3573-3587.e29 (2021).

62. Vlahos, L. *et al.* Systematic, Protein Activity-based Characterization of Single Cell State. doi:10.1101/2021.05.20.445002.

63. Wolf, F. A., Angerer, P. & Theis, F. J. SCANPY: Large-scale single-cell gene expression data analysis. *Genome Biol* **19**, (2018).

64. Barkas, N., Petukhov, V., Kharchenko, P. & Biederstedt, E. pagoda2: Single Cell Analysis and Differential Expression. Preprint at https://CRAN.R-project.org/package=pagoda2 (2022).

Acknowledgements

We would like to acknowledge Dr. J Heng from Remotely Consulting for the services provided in English-language editing of the manuscript, as well as for his valuable feedback on *Decipher*.